The Event Horizon Telescope image of the quasar NRAO 530

Jorstad, S.; Wielgus, M.; Lico, R.; Issaoun, S.; Broderick, A.E.; Pesce, D.W.; ... ; Zhao, S.-S.

The Astrophysical Journal, 943:170 (19pp), 2023 February 1 https://doi.org/10.3847/1538-4357/acaea8

The Event Horizon Telescope Image of the Quasar NRAO 530

Svetlana Jorstad[1], Maciek Wielgus[2], Rocco Lico[3,4], Sara Issaoun[5,6], Avery E. Broderick[7,8,9], Dominic W. Pesce[5,10], Jun Liu (刘俊)[2], Guang-Yao Zhao[3], Thomas P. Krichbaum[2], Lindy Blackburn[5,10], Chi-kwan Chan[11,12,13], Michael Janssen[2], Venkatessh Ramakrishnan[14,15,16], Kazunori Akiyama[10,17,18], Antxon Alberdi[3], Juan Carlos Algaba[19], Katherine L. Bouman[20], Ilje Cho[3], Antonio Fuentes[3], José L. Gómez[3], Mark Gurwell[5], Michael D. Johnson[5,10], Jae-Young Kim[2,21], Ru-Sen Lu (路如森)[2,22,23], Iván Martí-Vidal[24,25], Monika Moscibrodzka[26], Felix M. Pötzl[2,27], Efthalia Traianou[2,3], Ilse van Bemmel[28], Walter Alef[2], Richard Anantua[5,10,29], Keiichi Asada[30], Rebecca Azulay[2,24,25], Uwe Bach[2], Anne-Kathrin Baczko[2], David Ball[11], Mislav Baloković[31], John Barrett[17], Michi Bauböck[32], Bradford A. Benson[33,34], Dan Bintley[35,36], Raymond Blundell[5], Geoffrey C. Bower[37,38], Hope Boyce[39,40], Michael Bremer[41], Christiaan D. Brinkerink[26], Roger Brissenden[5,10], Silke Britzen[2], Dominique Broguiere[41], Thomas Bronzwaer[26], Sandra Bustamante[42], Do-Young Byun[43,44], John E. Carlstrom[34,45,46,47], Chiara Ceccobello[48], Andrew Chael[49], Koushik Chatterjee[5,10], Shami Chatterjee[50], Ming-Tang Chen[37], Yongjun Chen (陈永军)[22,23], Xiaopeng Cheng[43], Pierre Christian[51], Nicholas S. Conroy[5,52], John E. Conway[48], James M. Cordes[50], Thomas M. Crawford[34,45], Geoffrey B. Crew[17], Alejandro Cruz-Osorio[53], Yuzhu Cui (崔玉竹)[54,55,56], Jordy Davelaar[26,57,58], Mariafelicia De Laurentis[53,59,60], Roger Deane[61,62,63], Jessica Dempsey[35,36,64], Gregory Desvignes[2,65], Jason Dexter[66], Vedant Dhruv[32], Sheperd S. Doeleman[5,10], Sean Dougal[11], Sergio A. Dzib[2,41], Ralph P. Eatough[2,67], Razieh Emami[5], Heino Falcke[26], Joseph Farah[68,69], Vincent L. Fish[17], Ed Fomalont[70], H. Alyson Ford[11], Raquel Fraga-Encinas[26], William T. Freeman[71,72], Per Friberg[35,36], Christian M. Fromm[2,53,73], Peter Galison[10,74,75], Charles F. Gammie[32,52,76], Roberto García[41], Olivier Gentaz[41], Boris Georgiev[7,8,9], Ciriaco Goddi[77,78,79,80], Roman Gold[81], Arturo I. Gómez-Ruiz[82,83], Minfeng Gu (顾敏峰)[22,84], Kazuhiro Hada[55,56], Daryl Haggard[39,40], Kari Haworth[5], Michael H. Hecht[17], Ronald Hesper[85], Dirk Heumann[11], Luis C. Ho (何子山)[86,87], Paul Ho[30,35,36], Mareki Honma[55,56,88], Chih-Wei L. Huang[30], Lei Huang (黄磊)[22,84], David H. Hughes[82], Shiro Ikeda[18,89,90,91], C. M. Violette Impellizzeri[70,92], Makoto Inoue[30], David J. James[93], Buell T. Jannuzi[11], Britton Jeter[30], Wu Jiang (江悟)[22], Alejandra Jiménez-Rosales[26], Abhishek V. Joshi[32], Taehyun Jung[43,44], Mansour Karami[7,8], Ramesh Karuppusamy[2], Tomohisa Kawashima[94], Garrett K. Keating[5], Mark Kettenis[28], Dong-Jin Kim[2], Jongsoo Kim[43], Junhan Kim[20], Motoki Kino[18,95], Jun Yi Koay[30], Prashant Kocherlakota[53], Yutaro Kofuji[55,88], Shoko Koyama[30,96], Carsten Kramer[41], Michael Kramer[2], Cheng-Yu Kuo[30,97], Noemi La Bella[26], Tod R. Lauer[98], Daeyoung Lee[32], Sang-Sung Lee[43], Po Kin Leung[99], Aviad Levis[20], Zhiyuan Li (李志远)[100,101], Greg Lindahl[5], Michael Lindqvist[48], Mikhail Lisakov[2], Kuo Liu[2], Elisabetta Liuzzo[102], Wen-Ping Lo[30,103], Andrei P. Lobanov[2], Laurent Loinard[104,105], Colin J. Lonsdale[17], Nicholas R. MacDonald[2], Jirong Mao (毛基荣)[106,107,108], Nicola Marchili[2,102], Sera Markoff[109,110], Daniel P. Marrone[11], Alan P. Marscher[1], Satoki Matsushita[30], Lynn D. Matthews[17], Lia Medeiros[11,111,112], Karl M. Menten[2], Daniel Michalik[34,113], Izumi Mizuno[35,36], Yosuke Mizuno[53,54,114], James M. Moran[5,10], Kotaro Moriyama[17,53,55], Cornelia Müller[2,26], Alejandro Mus[24,25], Gibwa Musoke[26,109], Ioannis Myserlis[115], Andrew Nadolski[52], Hiroshi Nagai[18,56], Neil M. Nagar[14], Masanori Nakamura[30,116], Ramesh Narayan[5,10], Gopal Narayanan[42], Iniyan Natarajan[61,117], Antonios Nathanail[53,118], Santiago Navarro Fuentes[115], Joey Neilsen[119], Roberto Neri[41], Chunchong Ni[7,8,9], Aristeidis Noutsos[2], Michael A. Nowak[120], Junghwan Oh[121], Hiroki Okino[55,88], Héctor Olivares[26], Gisela N. Ortiz-León[2,105], Tomoaki Oyama[55], Feryal Özel[11], Daniel C. M. Palumbo[5,10], Georgios Filippos Paraschos[2], Jongho Park[30,122], Harriet Parsons[35,36], Nimesh Patel[5], Ue-Li Pen[7,30,123,124,125], Vincent Piétu[41], Richard Plambeck[126], Aleksandar PopStefanija[42], Oliver Porth[53,109], Ben Prather[32], Jorge A. Preciado-López[7], Dimitrios Psaltis[11], Hung-Yi Pu[30,127,128], Ramprasad Rao[5], Mark G. Rawlings[35,36,129], Alexander W. Raymond[5,10], Luciano Rezzolla[53,130,131], Angelo Ricarte[5,10], Bart Ripperda[6,58,112,132], Freek Roelofs[5,10,26], Alan Rogers[17], Eduardo Ros[2], Cristina Romero-Cañizales[30], Arash Roshaneshat[11], Helge Rottmann[2], Alan L. Roy[2], Ignacio Ruiz[115], Chet Ruszczyk[17], Kazi L. J. Rygl[102], Salvador Sánchez[115], David Sánchez-Argüelles[82,83], Miguel Sánchez-Portal[115], Mahito Sasada[55,133,134], Kaushik Satapathy[11], Tuomas Savolainen[2,16,135], F. Peter Schloerb[42], Jonathan Schonfeld[5], Karl-Friedrich Schuster[41], Lijing Shao[2,87], Zhiqiang Shen (沈志强)[22,23], Des Small[28], Bong Won Sohn[43,44,136], Jason SooHoo[17], Kamal Souccar[42], He Sun (孙赫)[20], Fumie Tazaki[55], Alexandra J. Tetarenko[6,137], Paul Tiede[5,10], Remo P. J. Tilanus[11,26,92,138], Michael Titus[17], Pablo Torne[2,115], Tyler Trent[11], Sascha Trippe[139], Matthew Turk[52], Huib Jan van Langevelde[28,92,140], Daniel R. van Rossum[26], Jesse Vos[26], Jan Wagner[2], Derek Ward-Thompson[141], John Wardle[142], Jonathan Weintroub[5,10], Norbert Wex[2], Robert Wharton[2], Kaj Wiik[143], Gunther Witzel[2], Michael F. Wondrak[26,144], George N. Wong[112,145], Qingwen Wu (吴庆文)[146], Paul Yamaguchi[5], Doosoo Yoon[109], André Young[26], Ken Young[5], Ziri Younsi[53,147], Feng Yuan (袁峰)[22,84,148], Ye-Fei Yuan (袁业飞)[149], J. Anton Zensus[2], Shuo Zhang[150], and Shan-Shan Zhao (赵杉杉)[22]

[1] Institute for Astrophysical Research, Boston University, 725 Commonwealth Avenue, Boston, MA 02215, USA; jorstad@bu.edu
[2] Max-Planck-Institut für Radioastronomie, Auf dem Hügel 69, D-53121 Bonn, Germany; maciek.wielgus@gmail.com
[3] Instituto de Astrofísica de Andalucía-CSIC, Glorieta de la Astronomía s/n, E-18008 Granada, Spain
[4] INAF-Istituto di Radioastronomia, Via P. Gobetti 101, I-40129 Bologna, Italy
[5] Center for Astrophysics, Harvard & Smithsonian, 60 Garden Street, Cambridge, MA 02138, USA
[6] NASA Hubble Fellowship Program, Einstein Fellow
[7] Perimeter Institute for Theoretical Physics, 31 Caroline Street North, Waterloo, ON, N2L 2Y5, Canada
[8] Department of Physics and Astronomy, University of Waterloo, 200 University Avenue West, Waterloo, ON, N2L 3G1, Canada
[9] Waterloo Centre for Astrophysics, University of Waterloo, Waterloo, ON, N2L 3G1, Canada
[10] Black Hole Initiative at Harvard University, 20 Garden Street, Cambridge, MA 02138, USA
[11] Steward Observatory and Department of Astronomy, University of Arizona, 933 N. Cherry Avenue, Tucson, AZ 85721, USA
[12] Data Science Institute, University of Arizona, 1230 N. Cherry Avenue, Tucson, AZ 85721, USA
[13] Program in Applied Mathematics, University of Arizona, 617 N. Santa Rita, Tucson, AZ 85721, USA
[14] Astronomy Department, Universidad de Concepción, Casilla 160-C, Concepción, Chile
[15] Finnish Centre for Astronomy with ESO, FI-20014 University of Turku, Finland
[16] Aalto University Metsähovi Radio Observatory, Metsähovintie 114, FI-02540 Kylmälä, Finland
[17] Massachusetts Institute of Technology Haystack Observatory, 99 Millstone Road, Westford, MA 01886, USA
[18] National Astronomical Observatory of Japan, 2-21-1 Osawa, Mitaka, Tokyo 181-8588, Japan
[19] Department of Physics, Faculty of Science, Universiti Malaya, 50603 Kuala Lumpur, Malaysia
[20] California Institute of Technology, 1200 East California Boulevard, Pasadena, CA 91125, USA
[21] Department of Astronomy and Atmospheric Sciences, Kyungpook National University, Daegu 702-701, Republic of Korea
[22] Shanghai Astronomical Observatory, Chinese Academy of Sciences, 80 Nandan Road, Shanghai 200030, People's Republic of China
[23] Key Laboratory of Radio Astronomy, Chinese Academy of Sciences, Nanjing 210008, People's Republic of China
[24] Departament d'Astronomia i Astrofísica, Universitat de València, C. Dr. Moliner 50, E-46100 Burjassot, València, Spain
[25] Observatori Astronòmic, Universitat de València, C. Catedrático José Beltrán 2, E-46980 Paterna, València, Spain
[26] Department of Astrophysics, Institute for Mathematics, Astrophysics and Particle Physics (IMAPP), Radboud University, P.O. Box 9010, 6500 GL Nijmegen, The Netherlands
[27] Institute of Astrophysics, Foundation for Research and Technology—Hellas, Voutes, 7110 Heraklion, Greece
[28] Joint Institute for VLBI ERIC (JIVE), Oude Hoogeveensedijk 4, 7991 PD Dwingeloo, The Netherlands
[29] Department of Physics & Astronomy, The University of Texas at San Antonio, One UTSA Circle, San Antonio, TX 78249, USA
[30] Institute of Astronomy and Astrophysics, Academia Sinica, 11F of Astronomy-Mathematics Building, AS/NTU No. 1, Sec. 4, Roosevelt Road, Taipei 10617, Taiwan, R.O.C.
[31] Yale Center for Astronomy & Astrophysics, Yale University, 52 Hillhouse Avenue, New Haven, CT 06511, USA
[32] Department of Physics, University of Illinois, 1110 West Green Street, Urbana, IL 61801, USA
[33] Fermi National Accelerator Laboratory, MS209, P.O. Box 500, Batavia, IL 60510, USA
[34] Department of Astronomy and Astrophysics, University of Chicago, 5640 South Ellis Avenue, Chicago, IL 60637, USA
[35] East Asian Observatory, 660 N. A'ohoku Place, Hilo, HI 96720, USA
[36] James Clerk Maxwell Telescope (JCMT), 660 N. A'ohoku Place, Hilo, HI 96720, USA
[37] Institute of Astronomy and Astrophysics, Academia Sinica, 645 N. A'ohoku Place, Hilo, HI 96720, USA
[38] Department of Physics and Astronomy, University of Hawaii at Manoa, 2505 Correa Road, Honolulu, HI 96822, USA
[39] Department of Physics, McGill University, 3600 rue University, Montréal, QC H3A 2T8, Canada
[40] McGill Space Institute, McGill University, 3550 rue University, Montréal, QC H3A 2A7, Canada
[41] Institut de Radioastronomie Millimétrique (IRAM), 300 rue de la Piscine, F-38406 Saint Martin d'Hères, France
[42] Department of Astronomy, University of Massachusetts, Amherst, MA 01003, USA
[43] Korea Astronomy and Space Science Institute, Daedeok-daero 776, Yuseong-gu, Daejeon 34055, Republic of Korea
[44] University of Science and Technology, Gajeong-ro 217, Yuseong-gu, Daejeon 34113, Republic of Korea
[45] Kavli Institute for Cosmological Physics, University of Chicago, 5640 South Ellis Avenue, Chicago, IL 60637, USA
[46] Department of Physics, University of Chicago, 5720 South Ellis Avenue, Chicago, IL 60637, USA
[47] Enrico Fermi Institute, University of Chicago, 5640 South Ellis Avenue, Chicago, IL 60637, USA
[48] Department of Space, Earth and Environment, Chalmers University of Technology, Onsala Space Observatory, SE-43992 Onsala, Sweden
[49] Princeton Gravity Initiative, Jadwin Hall, Princeton University, Princeton, NJ 08544, USA
[50] Cornell Center for Astrophysics and Planetary Science, Cornell University, Ithaca, NY 14853, USA
[51] Physics Department, Fairfield University, 1073 North Benson Road, Fairfield, CT 06824, USA
[52] Department of Astronomy, University of Illinois at Urbana-Champaign, 1002 West Green Street, Urbana, IL 61801, USA
[53] Institut für Theoretische Physik, Goethe-Universität Frankfurt, Max-von-Laue-Straße 1, D-60438 Frankfurt am Main, Germany
[54] Tsung-Dao Lee Institute, Shanghai Jiao Tong University, Shengrong Road 520, Shanghai, 201210, People's Republic of China
[55] Mizusawa VLBI Observatory, National Astronomical Observatory of Japan, 2-12 Hoshigaoka, Mizusawa, Oshu, Iwate 023-0861, Japan
[56] Department of Astronomical Science, The Graduate University for Advanced Studies (SOKENDAI), 2-21-1 Osawa, Mitaka, Tokyo 181-8588, Japan
[57] Department of Astronomy and Columbia Astrophysics Laboratory, Columbia University, 550 W 120th Street, New York, NY 10027, USA
[58] Center for Computational Astrophysics, Flatiron Institute, 162 Fifth Avenue, New York, NY 10010, USA
[59] Dipartimento di Fisica "E. Pancini,"Universitá di Napoli "Federico II," Compl. Univ. di Monte S. Angelo, Edificio G, Via Cinthia, I-80126, Napoli, Italy
[60] INFN Sez. di Napoli, Compl. Univ. di Monte S. Angelo, Edificio G, Via Cinthia, I-80126, Napoli, Italy
[61] Wits Centre for Astrophysics, University of the Witwatersrand, 1 Jan Smuts Avenue, Braamfontein, Johannesburg 2050, South Africa
[62] Department of Physics, University of Pretoria, Hatfield, Pretoria 0028, South Africa
[63] Centre for Radio Astronomy Techniques and Technologies, Department of Physics and Electronics, Rhodes University, Makhanda 6140, South Africa
[64] ASTRON, Oude Hoogeveensedijk 4, 7991 PD Dwingeloo, The Netherlands
[65] LESIA, Observatoire de Paris, Université PSL, CNRS, Sorbonne Université, Université de Paris, 5 place Jules Janssen, F-92195 Meudon, France
[66] JILA and Department of Astrophysical and Planetary Sciences, University of Colorado, Boulder, CO 80309, USA
[67] National Astronomical Observatories, Chinese Academy of Sciences, 20A Datun Road, Chaoyang District, Beijing 100101, People's Republic of China
[68] Las Cumbres Observatory, 6740 Cortona Drive, Suite 102, Goleta, CA 93117-5575, USA
[69] Department of Physics, University of California, Santa Barbara, CA 93106-9530, USA
[70] National Radio Astronomy Observatory, 520 Edgemont Road, Charlottesville, VA 22903, USA
[71] Department of Electrical Engineering and Computer Science, Massachusetts Institute of Technology, 32-D476, 77 Massachusetts Avenue, Cambridge, MA 02142, USA
[72] Google Research, 355 Main St., Cambridge, MA 02142, USA
[73] Institut für Theoretische Physik und Astrophysik, Universität Würzburg, Emil-Fischer-Str. 31, D-97074 Würzburg, Germany

[74] Department of History of Science, Harvard University, Cambridge, MA 02138, USA
[75] Department of Physics, Harvard University, Cambridge, MA 02138, USA
[76] NCSA, University of Illinois, 1205 W Clark St, Urbana, IL 61801, USA
[77] Universidade de Sao Paulo, Instituto de Astronomia, Geofísica e Ciencias Atmosféricas, Departamento de Astronomia, Sao Paulo, SP 05508-090, Brazil
[78] Dipartimento di Fisica, Università degli Studi di Cagliari, SP Monserrato-Sestu km 0.7, I-09042 Monserrato, Italy
[79] INAF—Osservatorio Astronomico di Cagliari, Via della Scienza 5, I-09047, Selargius, CA, Italy
[80] INFN, Sezione di Cagliari, Cittadella Univ., I-09042 Monserrato (CA), Italy
[81] CP3-Origins, University of Southern Denmark, Campusvej 55, DK-5230 Odense M, Denmark
[82] Instituto Nacional de Astrofísica, Óptica y Electrónica. Apartado Postal 51 y 216, 72000. Puebla Pue., México
[83] Consejo Nacional de Ciencia y Tecnologìa, Av. Insurgentes Sur 1582, 03940, Ciudad de México, México
[84] Key Laboratory for Research in Galaxies and Cosmology, Chinese Academy of Sciences, Shanghai 200030, People's Republic of China
[85] NOVA Submillimeter Instrumentation Group, Kapteyn Astronomical Institute, University of Groningen, Landleven 12, 9747 AD Groningen, The Netherlands
[86] Department of Astronomy, School of Physics, Peking University, Beijing 100871, People's Republic of China
[87] Kavli Institute for Astronomy and Astrophysics, Peking University, Beijing 100871, People's Republic of China
[88] Department of Astronomy, Graduate School of Science, The University of Tokyo, 7-3-1 Hongo, Bunkyo-ku, Tokyo 113-0033, Japan
[89] The Institute of Statistical Mathematics, 10-3 Midori-cho, Tachikawa, Tokyo, 190-8562, Japan
[90] Department of Statistical Science, The Graduate University for Advanced Studies (SOKENDAI), 10-3 Midori-cho, Tachikawa, Tokyo 190-8562, Japan
[91] Kavli Institute for the Physics and Mathematics of the Universe, The University of Tokyo, 5-1-5 Kashiwanoha, Kashiwa, 277-8583, Japan
[92] Leiden Observatory, Leiden University, Postbus 2300, 9513 RA Leiden, The Netherlands
[93] ASTRAVEO LLC, P.O. Box 1668, Gloucester, MA 01931, USA
[94] Institute for Cosmic Ray Research, The University of Tokyo, 5-1-5 Kashiwanoha, Kashiwa, Chiba 277-8582, Japan
[95] Kogakuin University of Technology & Engineering, Academic Support Center, 2665-1 Nakano, Hachioji, Tokyo 192-0015, Japan
[96] Niigata University, 8050 Ikarashi-nino-cho, Nishi-ku, Niigata 950-2181, Japan
[97] Physics Department, National Sun Yat-Sen University, No. 70, Lien-Hai Road, Kaosiung City 80424, Taiwan, R.O.C.
[98] National Optical Astronomy Observatory, 950 N. Cherry Avenue, Tucson, AZ 85719, USA
[99] Department of Physics, The Chinese University of Hong Kong, Shatin, N.T., Hong Kong
[100] School of Astronomy and Space Science, Nanjing University, Nanjing 210023, People's Republic of China
[101] Key Laboratory of Modern Astronomy and Astrophysics, Nanjing University, Nanjing 210023, People's Republic of China
[102] INAF-Istituto di Radioastronomia & Italian ALMA Regional Centre, Via P. Gobetti 101, I-40129 Bologna, Italy
[103] Department of Physics, National Taiwan University, No. 1, Sect. 4, Roosevelt Road, Taipei 10617, Taiwan, R.O.C.
[104] Instituto de Radioastronomía y Astrofísica, Universidad Nacional Autónoma de México, Morelia 58089, México
[105] Instituto de Astronomía, Universidad Nacional Autónoma de México (UNAM), Apdo Postal 70-264, Ciudad de México, México
[106] Yunnan Observatories, Chinese Academy of Sciences, 650011 Kunming, Yunnan Province, People's Republic of China
[107] Center for Astronomical Mega-Science, Chinese Academy of Sciences, 20A Datun Road, Chaoyang District, Beijing, 100012, People's Republic of China
[108] Key Laboratory for the Structure and Evolution of Celestial Objects, Chinese Academy of Sciences, 650011 Kunming, People's Republic of China
[109] Anton Pannekoek Institute for Astronomy, University of Amsterdam, Science Park 904, 1098 XH, Amsterdam, The Netherlands
[110] Gravitation and Astroparticle Physics Amsterdam (GRAPPA) Institute, University of Amsterdam, Science Park 904, 1098 XH Amsterdam, The Netherlands
[111] NSF Astronomy and Astrophysics Postdoctoral Fellow
[112] School of Natural Sciences, Institute for Advanced Study, 1 Einstein Drive, Princeton, NJ 08540, USA
[113] Science Support Office, Directorate of Science, European Space Research and Technology Centre (ESA/ESTEC), Keplerlaan 1, 2201 AZ Noordwijk, The Netherlands
[114] School of Physics and Astronomy, Shanghai Jiao Tong University, 800 Dongchuan Road, Shanghai, 200240, People's Republic of China
[115] Institut de Radioastronomie Millimétrique (IRAM), Avenida Divina Pastora 7, Local 20, E-18012, Granada, Spain
[116] National Institute of Technology, Hachinohe College, 16-1 Uwanotai, Tamonoki, Hachinohe City, Aomori 039-1192, Japan
[117] South African Radio Astronomy Observatory, Observatory 7925, Cape Town, South Africa
[118] Department of Physics, National and Kapodistrian University of Athens, Panepistimiopolis, GR 15783 Zografos, Greece
[119] Department of Physics, Villanova University, 800 Lancaster Avenue, Villanova, PA 19085, USA
[120] Physics Department, Washington University CB 1105, St Louis, MO 63130, USA
[121] Sejong University, 209 Neungdong-ro, Gwangjin-gu, Seoul, Republic of Korea
[122] EACOA Fellow
[123] Canadian Institute for Theoretical Astrophysics, University of Toronto, 60 St. George Street, Toronto, ON, M5S 3H8, Canada
[124] Dunlap Institute for Astronomy and Astrophysics, University of Toronto, 50 St. George Street, Toronto, ON, M5S 3H4, Canada
[125] Canadian Institute for Advanced Research, 180 Dundas Street West, Toronto, ON, M5G 1Z8, Canada
[126] Radio Astronomy Laboratory, University of California, Berkeley, CA 94720, USA
[127] Department of Physics, National Taiwan Normal University, No. 88, Sec.4, Tingzhou Road, Taipei 116, Taiwan, R.O.C.
[128] Center of Astronomy and Gravitation, National Taiwan Normal University, No. 88, Sec. 4, Tingzhou Road, Taipei 116, Taiwan, R.O.C.
[129] Gemini Observatory/NSF NOIRLab, 670 N. A'ohoku Place, Hilo, HI 96720, USA
[130] Frankfurt Institute for Advanced Studies, Ruth-Moufang-Strasse 1, D-60438 Frankfurt, Germany
[131] School of Mathematics, Trinity College, Dublin 2, Ireland
[132] Department of Astrophysical Sciences, Peyton Hall, Princeton University, Princeton, NJ 08544, USA
[133] Department of Physics, Tokyo Institute of Technology, 2-12-1 Ookayama, Meguro-ku, Tokyo 152-8551, Japan
[134] Hiroshima Astrophysical Science Center, Hiroshima University, 1-3-1 Kagamiyama, Higashi-Hiroshima, Hiroshima 739-8526, Japan
[135] Aalto University Department of Electronics and Nanoengineering, PL 15500, FI-00076 Aalto, Finland
[136] Department of Astronomy, Yonsei University, Yonsei-ro 50, Seodaemun-gu, 03722 Seoul, Republic of Korea
[137] Department of Physics and Astronomy, Texas Tech University, Lubbock, TX 79409-1051, USA
[138] Netherlands Organisation for Scientific Research (NWO), Postbus 93138, 2509 AC Den Haag, The Netherlands
[139] Department of Physics and Astronomy, Seoul National University, Gwanak-gu, Seoul 08826, Republic of Korea
[140] University of New Mexico, Department of Physics and Astronomy, Albuquerque, NM 87131, USA
[141] Jeremiah Horrocks Institute, University of Central Lancashire, Preston PR1 2HE, UK
[142] Physics Department, Brandeis University, 415 South Street, Waltham, MA 02453, USA
[143] Tuorla Observatory, Department of Physics and Astronomy, University of Turku, Finland
[144] Radboud Excellence Fellow of Radboud University, Nijmegen, The Netherlands
[145] Princeton Gravity Initiative, Princeton University, Princeton, NJ 08544, USA
[146] School of Physics, Huazhong University of Science and Technology, Wuhan, Hubei, 430074, People's Republic of China
[147] Mullard Space Science Laboratory, University College London, Holmbury St. Mary, Dorking, Surrey, RH5 6NT, UK
[148] School of Astronomy and Space Sciences, University of Chinese Academy of Sciences, No. 19A Yuquan Road, Beijing 100049, People's Republic of China

[149] Astronomy Department, University of Science and Technology of China, Hefei 230026, People's Republic of China
[150] Bard College, 30 Campus Road, Annandale-on-Hudson, NY 12504, USA
Received 2022 November 3; revised 2022 December 20; accepted 2022 December 22; published 2023 February 7

Abstract

We report on the observations of the quasar NRAO 530 with the Event Horizon Telescope (EHT) on 2017 April 5−7, when NRAO 530 was used as a calibrator for the EHT observations of Sagittarius A*. At $z = 0.902$, this is the most distant object imaged by the EHT so far. We reconstruct the first images of the source at 230 GHz, at an unprecedented angular resolution of ∼20 μas, both in total intensity and in linear polarization (LP). We do not detect source variability, allowing us to represent the whole data set with static images. The images reveal a bright feature located on the southern end of the jet, which we associate with the core. The feature is linearly polarized, with a fractional polarization of ∼5%–8%, and it has a substructure consisting of two components. Their observed brightness temperature suggests that the energy density of the jet is dominated by the magnetic field. The jet extends over 60 μas along a position angle ∼ −28°. It includes two features with orthogonal directions of polarization (electric vector position angle), parallel and perpendicular to the jet axis, consistent with a helical structure of the magnetic field in the jet. The outermost feature has a particularly high degree of LP, suggestive of a nearly uniform magnetic field. Future EHT observations will probe the variability of the jet structure on microarcsecond scales, while simultaneous multiwavelength monitoring will provide insight into the high-energy emission origin.

Unified Astronomy Thesaurus concepts: Extragalactic astronomy (506)

1. Introduction

NRAO 530 (1730−130, J1733−1304) is a flat-spectrum radio quasar (FSRQ) that belongs to the class of bright γ-ray blazars and shows significant variability across the entire electromagnetic spectrum. The source was monitored by the University of Michigan Radio Observatory at 4.8, 8.4, and 14.5 GHz for several decades[151] until 2012. The quasar underwent a dramatic radio outburst in 1997 (Aller et al. 2009), during which its flux density at 14.5 GHz exceeded 10 Jy, while the average value is ∼2 Jy. Since 2002, NRAO 530 has been monitored by the Submillimeter Array (SMA; Maunakea, Hawaii) at 1.3 mm and 870 μm.[152] The data show high amplitude variability at 1.3 mm from 1–4 Jy, with the brightest outburst in the end of 2010 contemporaneous with prominent γ-ray activity (Williamson et al. 2014). Ramakrishnan et al. (2015) found a statistically significant correlation between the radio and γ-ray light curves of NRAO 530, based on measurements at 37 GHz by the Metsähovi Radio Observatory (Aalto University, Finland) and γ-ray fluxes measured with the Large Area Telescope (LAT) on board the Fermi Space Gamma-Ray Telescope. The blazar is included in a sample of active galactic nuclei (AGNs) observed with the POLAMI program (Agudo et al. 2014), which provides both the flux density and polarization measurements at 3 mm and 1.3 mm started in 2009. According to the data during the perion 2007–2021, the degree of linear polarization (LP) at 1.3 mm changes from 1% to 15%, with circular polarization detections at a level of 1%–2% (private communication).

The quasar is known as a violently variable object at optical wavelengths. According to the SMARTS optical/IR monitoring program of blazars (Bonning et al. 2012), NRAO 530 has a fractional variability amplitude of ∼68% and ∼35% at optical and IR wavelengths, respectively, with an average magnitude of ∼14 at the K band ($\lambda_{\rm eff} \sim 2.2\,\mu$m) and ∼17.5 in the R band ($\lambda_{\rm eff} \sim 658$ nm). Foschini et al. (2006) reported a short hard X-ray flare detected serendipitously by the IBIS/ISGRI detector on board INTEGRAL on 2004 February 17, although the timescale of the flare, <1 hr, questions the association with the FSRQ. However, a moderate increase of the LP at 2 cm contemporaneous with the flare was observed as well. The recent 10 yr Fermi LAT catalog, 4FGL (Abdollahi et al. 2020), lists the average γ-ray flux of the source at 0.1–300 GeV as $(1.8 \pm 1.2) \times 10^{-7}$ phot cm^{-2} s^{-1}. During this period NRAO 530 underwent the highest amplitude γ-ray outburst in 2010 October–November, when the γ-ray flux rose to 10^{-6} phot cm^{-2} s^{-1} (Williamson et al. 2014). This γ-ray activity coincided with a significant brightening at optical wavelengths and an increase of the optical linear degree of polarization up to 15%.[153]

NRAO 530 possesses a highly relativistic jet. The source is intensively monitored with the Very Long Baseline Array (VLBA) at 15 GHz within the MOJAVE program (e.g., Lister et al. 2016) and at 43 GHz within the VLBA-BU-BLAZAR program (Jorstad et al. 2017; Weaver et al. 2022). VLBA images show a radio jet dominated by the core located at the southern end of the jet. At 15 GHz, the jet extends up to 10 mas to the north, with a weak feature observed ∼25 mas from the core. Based on 11 moving features, Lister et al. (2019) reported a median apparent speed of $12.3 \pm 0.6\,c$, with a maximum apparent speed of $27.3 \pm 1.0\,c$. At 43 GHz, the jet contains a stationary feature located ∼0.3 mas from the core and curves to the northwest ∼0.8 mas from the core. Eight moving knots detected at 43 GHz over 2007–2018 exhibit a wide range of apparent speeds, from $2.6 \pm 0.5\,c$ to $37.2 \pm 0.2\,c$ (Weaver et al. 2022), with three knots revealing a strong acceleration after passing the stationary feature, while knot B3 ejected in the beginning of 2010 demonstrates both accelerations from 4.1 c to 7.7 c and to 33.7 c and then a deceleration to 8.5 c. Using properties of the light curves of moving knots and their apparent speeds, Jorstad et al. (2017) estimated the average Lorentz and Doppler factors of the jet to be $\Gamma \sim 8$ and $\delta \sim 9$, respectively, with a jet viewing angle of ∼3°. These values of

[151] https://dept.astro.lsaumich.edu/data sets/umrao.php
[152] http://sma1.sma.hawaii.edu/callist/callist.html?plot=1733-130
[153] http://www.bu.edu/blazars/VLBA_GLAST/1730.html

the Lorentz and Doppler factors are close to the minimum values obtained by Liodakis et al. (2018) for the jet of NRAO 530. These authors estimated the variability of the Doppler factor by analyzing the 15 GHz light curve provided by the Owens Valley 40 m Radio Telescope after taking into consideration brightness temperature arguments and the apparent speeds of knots at 15 GHz; this resulted in $\Gamma_{\rm max} \sim 40$ and $\delta_{\rm max} \sim 21$.

On kiloparsec scales, the quasar shows a weak two-sided jet elongated in the east–west direction over 2.″5, with a very diffuse eastern part and a bright, compact knot on the western side, located about 1″ from the core (Kharb et al. 2010). The kiloparsec-scale jet is almost perpendicular to the parsec-scale jet and has a complex radio morphology: the eastern part is similar to that expected for Fanaroff–Riley I (FRI) type radio galaxies, while the western part can be classified as FRII type.

NRAO 530 has a redshift of $z = 0.902$ (Junkkarinen 1984), for which 100 μas corresponds to a linear distance of 0.803 pc (Planck Collaboration et al. 2016, $H_0 = 67.7$ km s^{-1} Mpc^{-1}, $\Omega_m = 0.307$, and $\Omega_\Lambda = 0.693$). The source contains a supermassive black hole, the mass of which is currently uncertain, with estimates ranging from $3 \times 10^8 M_\odot$ (Keck 2019) to $2 \times 10^9 M_\odot$ (Liang & Liu 2003).

Due to its brightness, compactness, and close location on the sky to the Galactic Center, NRAO 530 is frequently used as a calibrator in very long baseline interferometry (VLBI) observations of the radio source Sagittarius A* (Sgr A*) located in the center of the Milky Way (e.g., Lu et al. 2011). In this paper we report on the VLBI observations of NRAO 530 in 2017 April, when the source was employed as a calibrator during the Event Horizon Telescope (EHT) observation of Sgr A* at 1.3 mm (EHTC et al. 2022a). During the EHT observation, NRAO 530 was in a moderate activity state at γ-ray energies with the flux $\sim 1 \times 10^{-7}$ phot cm^{-2} s^{-1} as well as at optical (R-band magnitude $\sim$17.8)[154] and radio wavelengths (the flux density at 37 GHz $\sim$3.7 Jy).[155] According to the VLBA monitorings at 43 GHz (Weaver et al. 2022) and 15 GHz (Lister et al. 2019), no superluminal components were ejected in 2017. The EHT observation of NRAO 530 provides unique insight into the subparsec scale structure of the quasar with microarcsecond resolution, which are important for understanding the blazar physics in general and properties of the NRAO 530 jet in particular. The outline of the paper is as follows: in Section 2 we describe the EHT observations of NRAO 530, their reduction and general data set properties, in Sections 3 and 4 we present results of total intensity and LP imaging, respectively, in Section 5 we discuss our results, and in Section 6 we summarize our findings.

2. Observations and Data Calibration

The EHT observed NRAO 530 on three consecutive nights on April 5–7 during the 2017 campaign (MJD 57848–57850), as a calibrator of Sgr A* (EHTC et al. 2022a, 2022b). The observations were performed with the full EHT 2017 array of eight telescopes located at six geographical sites: the Atacama Large Millimeter/submillimeter Array (ALMA)[156] and the Atacama Pathfinder Experiment (APEX) telescope in Chile; the Large Millimeter Telescope Alfonso Serrano (LMT) in Mexico; the IRAM 30 m telescope (PV, joined only on April 7) in Spain; the Submillimeter Telescope (SMT) in Arizona; the James Clerk Maxwell Telescope (JCMT) and SMA in Hawaii; and the South Pole Telescope (SPT) in Antarctica. Two 2 GHz wide frequency bands, centered at 227.1 GHz (LO), and 229.1 GHz (H I), were recorded. The observations were carried out using dual feeds, right-hand and left-hand circularly polarized (RCP ad LCP, respectively), for all stations other than ALMA and JCMT. ALMA recorded dual LP, which was subsequently converted at the correlation stage to a circular basis by `PolConvert` (Martí-Vidal et al. 2016; Goddi et al. 2019). The JCMT only observed the RCP component, which we utilized to approximate total intensity (this approximation is correct as long as the fractional circular polarization of the source can be neglected), and we typically omit JCMT baselines for the polarimetric imaging. The EHT array setup is detailed in EHTC et al. (2019a, 2019b).

Recorded signals were correlated at the MIT Haystack Observatory and the Max-Planck-Institut für Radioastronomie, Bonn. Subsequent data reduction procedures are described in EHTC et al. (2019c), Blackburn et al. (2019), and Janssen et al. (2019). There were minor updates to the calibration with respect to the EHT results published earlier (EHTC et al. 2019a; Kim et al. 2020), particularly regarding the telescope sensitivity estimates and complex polarimetric gains calibration. These updates are identical to those described in the EHT Sgr A* publications (EHTC et al. 2022a, 2022b). Flux density on the short intra-site baselines (ALMA-APEX and SMA-JCMT) was gain-calibrated to the simultaneous ALMA-only flux density of 1.6 Jy, reported by Goddi et al. (2021), providing an additional constraint on the amplitude gains for the stations with a colocated partner (network calibration; Blackburn et al. 2019). The polarimetric leakage calibration follows procedures outlined in EHTC et al. (2021), where D-terms of stations with an intra-site VLBI baseline (ALMA, APEX, SMA, and JCMT) were calculated through a multi-source fitting procedure (Martí-Vidal et al. 2021), and several estimates for D-terms of remaining stations were reported. Here we employ the fiducial D-terms given by Issaoun et al. (2022) based on the analysis presented in EHTC et al. (2021). Some imaging algorithms that we use ignore the leakage calibration and estimate D-terms independently, providing an additional consistency check of the calibration procedures and their impact on the resulting images (see Section 3).

The (u, v)-coverage of the EHT observations of NRAO 530 is given in Figure 1. We show the coverage on each individual day, as well as aggregated over the entire observing campaign. The longest projected baseline reaches 8.66 Gλ for SPT-PV, which determines the instrumental angular resolution of 24 μas, measured as the minimum fringe spacing. Inspection of the data revealed no indication of the source structure evolution during the observations spanning only about 52 hr on 2017 April 5−7, with the total on-source integration time of 76 minutes (see Figures 2–3). For that reason, the entire data set was used simultaneously for static imaging and model fitting.

The NRAO 530 data set self-consistency has been rigorously verified as a validation of the EHT Sgr A* results, presented in EHTC et al. (2022b). The signal-to-noise ratio (S/N) of individual NRAO 530 detections (band-averaged in frequency, scan-averaged in time) typically exceeds 100 on baselines to

[154] http://www.bu.edu/blazars/VLBA_GLAST/1730.html

[155] http://www.metsahovi.fi/AGN/data/

[156] ALMA joined on April 6 and 7, operating as a phased array of, on average, 37 dishes of 12 m diameter, in a compact configuration with the longest baselines not exceeding 300 m in length (Goddi et al. 2019; Wielgus et al. 2022).

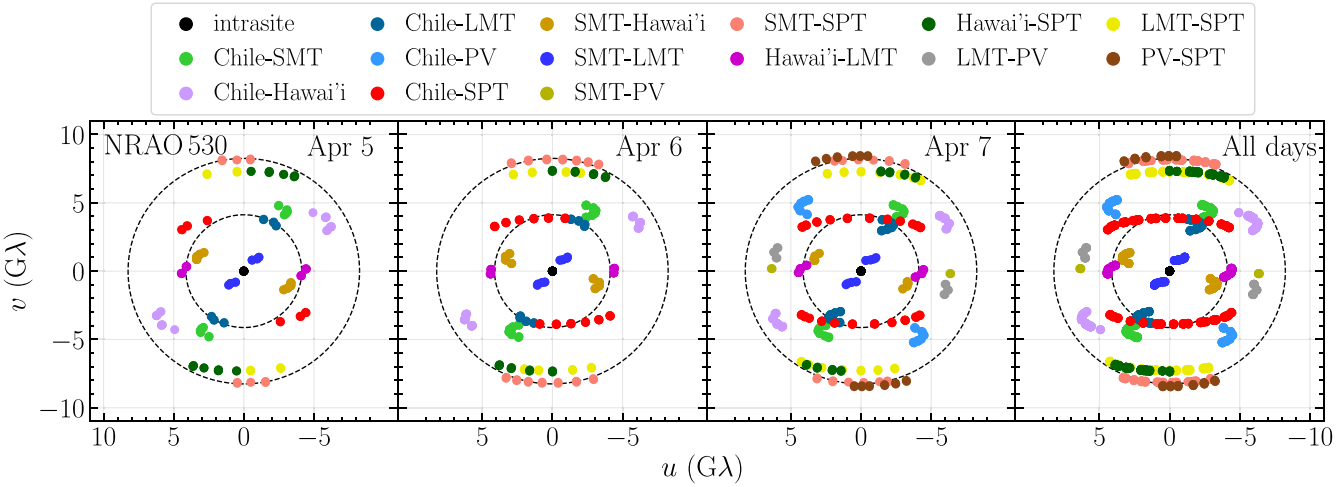

Figure 1. EHT (u, v)-coverage of the NRAO 530 observations on 2017 April 5, 6, and 7, and all days aggregated. Each colored point corresponds to a single VLBI scan of 3–4 minutes. ALMA participated in the observations on 2017 April 6 and 7. Dashed circles indicate the fringe spacing of 50 and 25 μas. "Chile" represents the stations ALMA and APEX. "Hawaii" represents the stations SMA and JCMT.

ALMA, and is about an order of magnitude lower on remaining baselines; see the top panel of Figure 2. We estimated an additional 2% of complex visibility uncertainties due to variety of nonclosing effects (e.g., residual polarimetric leakage, frequency, and time smearing); see EHTC et al. (2019c, 2022b). Inspecting the calibrated visibility amplitudes in the middle panel of Figure 2, we notice that the shortest inter-site baseline (LMT-SMT) provides a lower limit on the compact emission flux density corresponding to about 0.6 Jy, which implies the presence of up to 1 Jy of milliarcsecond-scale flux that is resolved out by the EHT but measured on the intra-site VLBI baselines and by the ALMA-only observations. Additionally, in the bottom panel of Figure 2 we present the measured visibility amplitudes as a function of the baseline length, projected at the jet PA (see Section 3). We notice that the amplitudes on baselines shorter than about 2.5 Gλ can be approximated by a Gaussian of FWHM 55 μas and 0.6 Jy amplitude, roughly informing us about the size and the total flux density of the observed compact feature. Measurements on baselines longer than 2.5 Gλ indicate a deviation from the Gaussian model, in agreement with the resolved source consisting of more than one component. Both EHT Sgr A* calibrators, NRAO 530 and J1924-2914 (Issaoun et al. 2022) are fairly compact and bright sources at 230 GHz. During the week-long EHT observing run, their source structure and flux density did not show significant variations (see Figure 3). These properties allowed us to use both sources for quantifying the effects of the residual errors in the characterization of the antenna gains. Mitigating such effects was crucial for discerning between the rapid intrinsic variability of Sgr A* and the apparent flux density variations produced by imperfect calibration (EHTC et al. 2022c, 2022d; Wielgus et al. 2022). Details about the procedures and methods used to obtain the antenna gains from the two calibrators and the subsequent transfer to the Sgr A* data sets are reported in Section 3.2 in EHTC et al. (2022b).

3. Total Intensity Imaging

For the imaging of NRAO 530, we have utilized data calibrated by the `EHT-HOPS` pipeline (Blackburn et al. 2019), combined over all days (2017 April 5–7) and both frequency bands (227.1 and 229.1 GHz). Nonzero closure phases shown in Figure 3 reveal resolved and nontrivial structure of the source. We used three analysis methods across five different implementations. These are: imaging via inverse modeling (the traditional CLEAN method), forward regularized maximum likelihood (RML) modeling (`eht-imaging` and `SMILI` algorithms), which are described in detail in EHTC et al. (2019d), as well as two posterior exploration methods based on a Markov Chain Monte Carlo (MCMC) scheme—a D-term Modeling Code (`DMC`; Pesce 2021) and a dedicated Bayesian image reconstruction framework `Themis` (Broderick et al. 2020a). For each of the methods, the freedom to decide resolution, field of view, or amount of data coherent averaging was left to the expert imaging subteams, who made such decisions based on the specific properties of each algorithm. As an example, MCMC methods tend to average data more to reduce the computational complexity of the likelihood evaluation. Below we give a short description of each method, with some details on the particular application to the NRAO 530 imaging.

3.1. `DIFMAP`

For CLEAN imaging, we have used the `DIFMAP` software package (Shepherd 1997). We have constructed multiple manual images prior to the final process to obtain a set of CLEAN windows corresponding to the source structure and agreeing best with the data. This window set includes a large circular Gaussian with a radius of 1 mas, located in the center of the map, which models the large-scale extended emission present in the source. The standard process of multiple consecutive CLEAN iterations, along with self-calibration procedures, was employed to achieve the best normalized χ^2 values between the data and the model for the closure phases, closure amplitudes, and visibilities. We have used data averaged in 10 s segments, a field of view of 1024×1024 pixels with a pixel size of 2 μas, and uniform weighting to optimize the image resolution.

3.2. `eht-imaging`

The `eht-imaging` code (Chael et al. 2016, 2018) implements the RML-based approach to imaging. In this

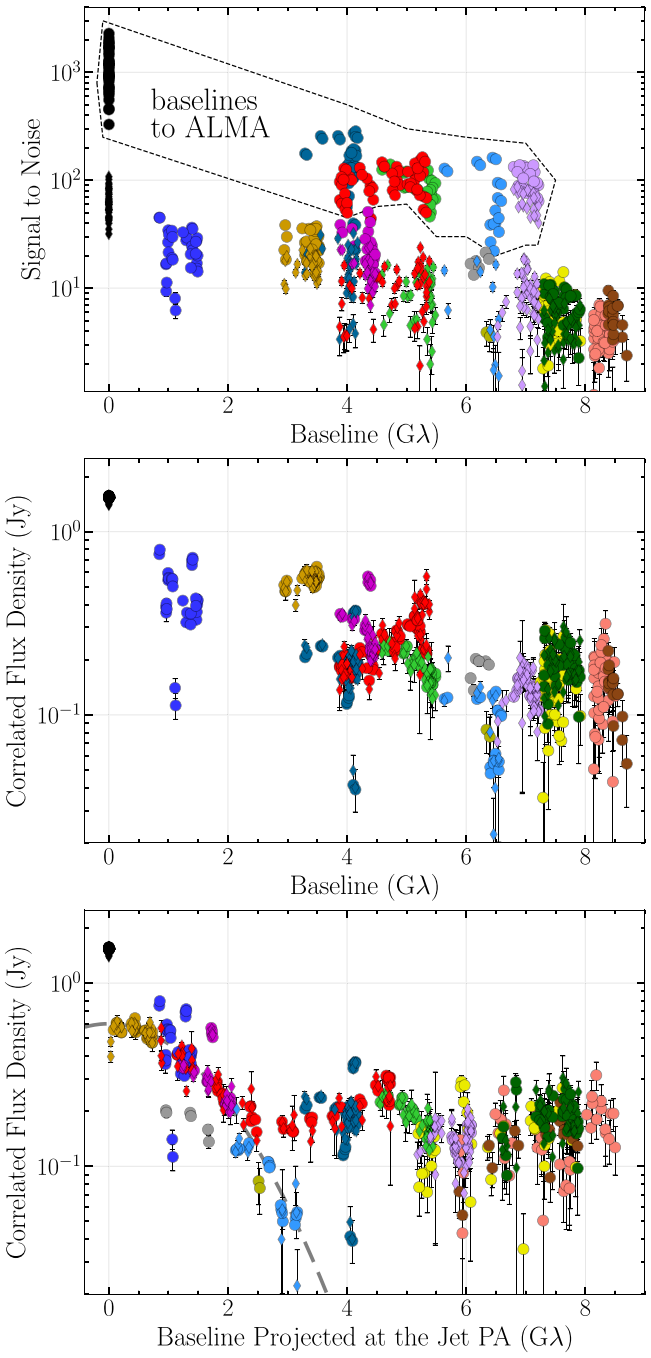

Figure 2. Top: signal-to-noise ratio (S/N) of NRAO 530 detections. Colors follow the convention of Figure 1. The entire data set (2017 April 5–7, both frequency bands) is shown. The data were averaged coherently in 240 s intervals. The circles denote primary baselines, while the diamonds denote redundant baselines (i.e., obtained with APEX or JCMT, rather than with ALMA or SMA). The cluster of S/N > 100 circles corresponds to ALMA baselines. Middle: the same as the top panel, but for the correlated flux densities (visibility amplitudes) in the a priori calibrated data set. Bottom: visibility amplitudes as a function of baseline length projected at the jet position angle (PA) of −25 deg (see Section 3). The dashed line represents a Gaussian component of FWHM 55 μas and 0.6 Jy amplitude.

method, an updated image is being proposed at every iteration, while the algorithm optimizes a cost function comprising the error term describing consistency with the data (predominantly through closure phases and log closure amplitudes; Blackburn et al. 2020), and regularization terms, similar to Bayesian priors. The latter may promote image properties such as smoothness, sparsity, compactness, or consistency with the imaging prior—here chosen to be a 60 μas FWHM circular Gaussian. For the NRAO 530 analysis, we assumed a field of view of 200 μas and a 64×64 pixel grid, and used scan-averaged data. The algorithm proceeds with an iterative sequence of gain calibration and cost function optimization.

3.3. SMILI

SMILI (Akiyama et al. 2017) is another RML imaging library that reconstructs interferometric images utilizing a similar set of regularizers including weighted-ℓ_1 (ℓ_1^w), total variation, total squared variation, and the maximum entropy regularizer. Prior to the imaging, we rescale the intra-site baseline flux density of NRAO 530 to 0.9 Jy to remove the contributions from the large-scale extended emission. During the imaging, we adopt a field of view of 300 μas and a 150×150 pixel grid, initializing the algorithm with a circular Gaussian prior, and using 10 s averaged data set. Subsequently, the imaging algorithm minimizes the regularized cost function. After 1000 iterations, self-calibration of the stations gains is performed, and the image prior is updated. This imaging and self-calibration loop is repeated until the reconstruction converges.

3.4. DMC

DMC formulates the imaging problem in terms of posterior exploration, which is carried out using a Hamiltonian Monte Carlo sampler as implemented in the PyMC3 Python package (Salvatier et al. 2016). The output of DMC is a collection of samples from the joint posterior over the image structure and calibration quantities. Rather than carrying out an iterative self-calibration procedure, DMC fits the complex gains at every station simultaneously with the full Stokes image structure. For NRAO 530 imaging, a field of view of 300 μas and a 30×30 pixel grid were used, the data were scan-averaged, and D-terms were fixed following Issaoun et al. (2022). A comprehensive description of the DMC model and implementation can be found in Pesce (2021).

3.5. Themis

Themis is a framework for fitting VLBI data with an MCMC posterior space exploration method (Broderick et al. 2020a). For NRAO 530 data analysis, the image was modeled with a spline raster defined using 6×5 control points, and an adaptively selected field of view (Broderick et al. 2020b). The data were scan-averaged. We solved for D-terms with Themis in order to provide a consistency test for the fiducial D-terms of EHTC et al. (2021) and Issaoun et al. (2022); see Section 4.1.

3.6. Fiducial Images of NRAO 530

Figure 4 presents final (fiducial) total intensity images obtained by the methods discussed in Sections 3.2–3.5. For the presentation purposes, all images are shown using the same field of view of 128×128 μas, more narrow than the field of view typically used for the imaging. The contribution of emission outside of this region is relatively small and consistent with the image noise level, which, in the case of the EHT, is rather high and dominated by the systematic uncertainties related to sparse (u, v)-coverage. There is a high degree of

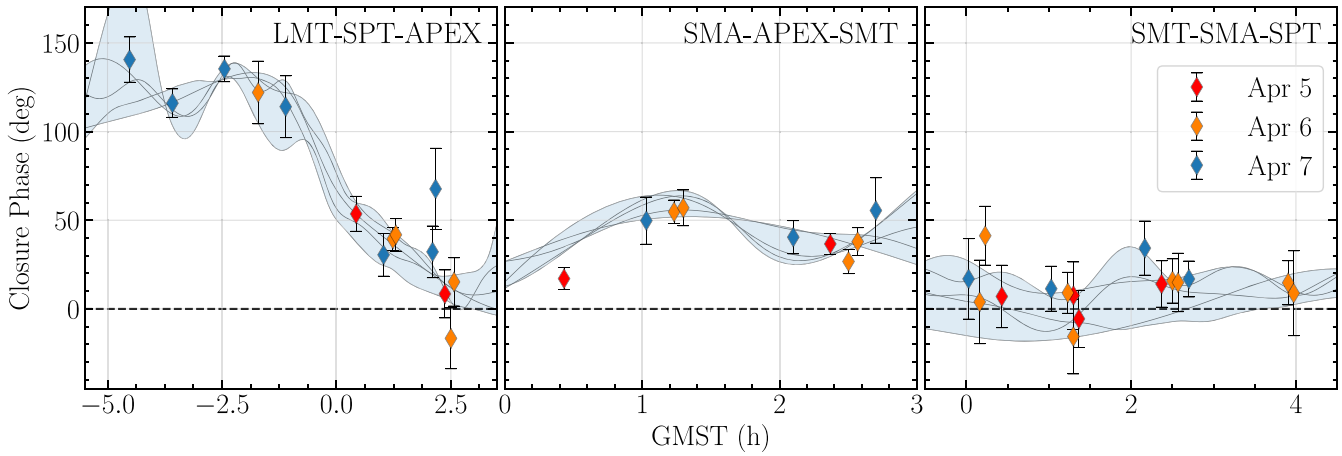

Figure 3. NRAO 530 closure phases measured on a selected nontrivial triangles. LO band data points averaged in 240 s intervals are shown. There is no statistically significant indication of structural variation between the three consecutive observing days. Predictions of the models obtained with a variety of imaging algorithms, discussed in Section 3, are indicated with thin black lines. The blue-shaded region indicates the range of predictions from different reconstructions presented in this paper.

agreement between the different imaging methods in terms of the source structure and the relative brightness of individual features. All images show the jet to be elongated from the southeast to the northwest over ∼60 μas. A visual inspection suggests that the jet consists of two dominant features (see Figure 5), with the brightest one, C0, located at the southeast end of the jet and itself exhibiting substructures C0a and C0b. However, there is also a difference between the models—DIFMAP and DMC images contain a very low-brightness extended feature that turns to the northeast, almost by ∼90° to the main direction of the jet, the eht-imaging image shows a hint of such a feature, while the SMILI and Themis methods do not reveal its presence. This discrepancy is likely related to the latter two algorithms promoting sparsity and compactness in the reconstructed images. We have designated this ambiguous feature as C2 in Figure 5, marked by a dashed line ellipse. Although the knot appears in the fiducial method-averaged image if we increase the dynamic range, its brightness peak is on the level of the image noise. In addition, DIFMAP, eht-imaging, and SMILI images correspond to very similar peak brightness values, but the Themis and DMC images indicate somewhat brighter and weaker brightness peaks, respectively.

Figure 3 shows consistency between closure phase measurements on selected triangles and corresponding predictions of the fitted models. Table 1 provides goodness of fit normalized χ^2 statistics computed for the models shown in Figure 4 for self-calibrated visibility amplitudes ($\chi^2_{\rm AMP}$), closure phases ($\chi^2_{\rm CP}$), and log closure amplitudes ($\chi^2_{\rm logCA}$). The estimated total flux density of the compact source model is also provided. This quantity is particularly challenging to constrain with the EHT array, which in 2017 lacked baselines between 5 Mλ and 500 Mλ projected length, sensitive to milliarcsecond-scale emission. Based on the presented statistics, there is no strong preference for any particular model. Therefore, we have combined the final images constructed by the different methods, shown in Figure 4, to produce a fiducial method-averaged total intensity image of NRAO 530, presented in Figure 5. The averaging procedure involves aligning images to maximize their cross-correlation, re-gridding them to a common resolution and field of view, and taking a standard arithmetic mean on a pixel-by-pixel basis. It follows the practice of EHTC et al. (2019d, 2022c), Kim et al. (2020), and Issaoun et al. (2022), and it is designed to make the resulting image-domain morphology more robust against method-specific systematics.

3.7. Total Intensity Component Modeling

We have modeled the visibilities, calibrated to the fiducial image, with circular Gaussian components using the task *modelfit* in DIFMAP. We also fitted a Gaussian model to the data in the eht-imaging framework, using closure-only data products to constrain the resolved source structure. In the latter case, the simplest model representing data properties sufficiently well consisted of a single elliptical and three circular Gaussian components. Each component (knot) is characterized by a flux density S at distance R from the center of the image with the relative R.A. and decl. equal to (0, 0), located at the flux density peak of the image, a position angle Θ with respect to the image center measured from north to east, and a size a corresponding to the FWHM of the Gaussian brightness distribution. Additionally, we performed modeling of the NRAO 530 eht-imaging results by fitting elliptical Gaussian components to the image-domain features. Table 2 gives the results of these three separate fitting procedures. To estimate uncertainties of components' parameters, we have used an approach employed in high-frequency VLBI, e.g., Jorstad et al. (2005): the flux density uncertainties correspond to either 10% of the flux density measurement or the noise level of the map obtained as the result of the *modelfit* task in DIFMAP depending on whatever is higher, while the position uncertainties are calculated as one-fifth of the synthetic CLEAN beam corresponding to the (u, v)-coverage for compact components, or equal to the beam size for diffuse knots with a size larger than the size of the beam.

The source consists of two main components, C0 and C1, as indicated in Figure 5. The knots are separated by ∼30 μas, with C0 being a factor of ∼3 brighter than C1. We associate C0 with the core of NRAO 530 at 1.3 mm and determine the jet direction on microarcsecond-scales to be ∼−28° east of north. All images shown in Figure 4 indicate nontrivial structure in C0, elongated along the jet axis. The models super-resolve the substructure of C0 into components C0a and C0b. In the case of DIFMAP, the model yields the best fit to C0b as a point

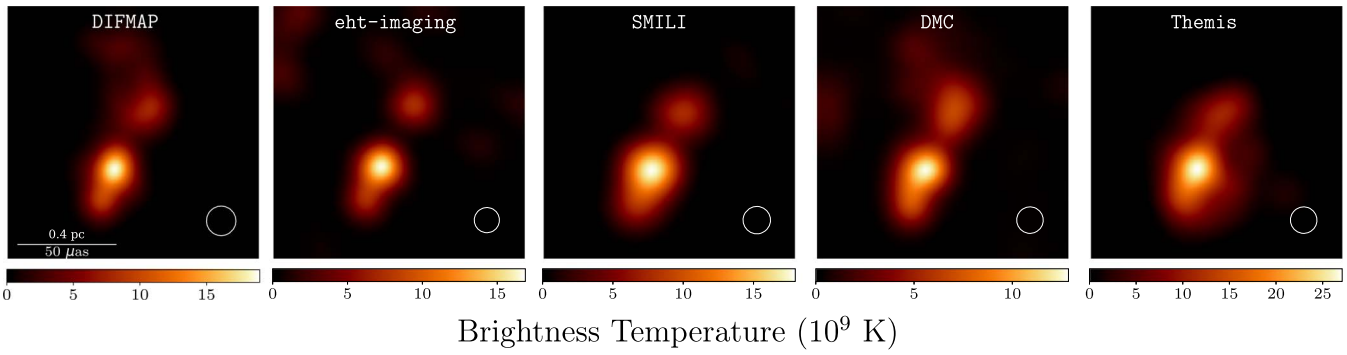

Figure 4. Images of NRAO 530 from the 2017 April EHT observations produced using DIFMAP, eht-imaging, SMILI, DMC, and Themis, shown within the adopted field of view of 128 μas. To simplify visual comparisons, the models were blurred to similar effective resolutions $\sim$15 μas, indicated in the bottom-right corner of each image.

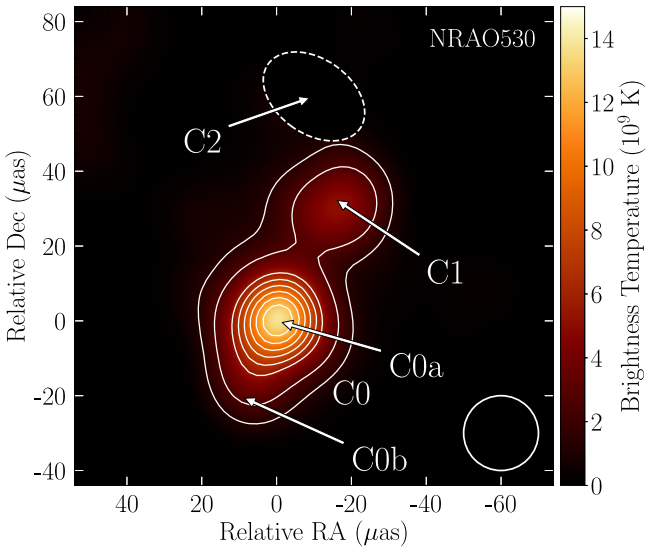

Figure 5. Fiducial EHT total intensity image of NRAO 530; the color scale corresponds to the brightness temperature; the contours represent the total intensity, with a peak value of 1.4×10^{10} K, starting at 10% of the peak and increasing in steps of 10%; the circle in the bottom-right corner shows the size of the nominal EHT beam with an FWHM diameter of 20 μas. The C2 contour is shown with a dashed line as it is below the 10% level of peak total intensity in the averaged image.

Table 1
Characterization of the Fits to NRAO 530 Data

Quantity	DIFMAP	eht-imaging	SMILI	DMC	Themis
$\chi^2_{\rm AMP}$	0.974	0.638	0.858	0.517	1.211
$\chi^2_{\rm CP}$	3.812	0.899	2.346	0.977	4.210
$\chi^2_{\rm logCA}$	1.513	1.137	2.727	0.943	2.844
Flux (Jy)	1.030	0.958	0.899	1.585	1.120

Note. For the χ^2 calculation, the original thermal error budget was inflated by a nonclosing systematic error amounting to 2% of the complex visibilities.

source. We interpret the brighter component C0a as the VLBI core. The weaker component C0b is located $\sim$20 μas southeast from the C0a core, along the same jet axis as the C0a and C1 components. Taking into account a small viewing angle of the jet, it is very unlikely that C0b is a counter-jet component. Instead, we interpret C0b as the result of the opacity stratification in the core, with C0b representing the more optically thick part of the jet. The Gaussian component fits

Table 2
Parameters of Total Intensity Components

Knot (1)	S (mJy) (2)	R (μas) (3)	Θ (deg) (4)	a (μas) (5)	$T_{\rm b}$ (10^{10} K) (6)
DIFMAP (Gaussian modeling)					
C0a	278 ± 29	1.8 ± 4	85.6 ± 71	16.3 ± 4.2	2.3
C0b	61 ± 15	21.9 ± 4	149.6 ± 13	0.0	
C1	124 ± 15	35.1 ± 5	-26.9 ± 9	15.0 ± 3.8	1.3
C2	106 ± 53	57.5 ± 20	-5.2 ± 24	33 ± 16	0.2
BG	871	1.8	46.8	1000	...
eht-imaging (Gaussian modeling)					
C0a	210	0.0	...	10.6	4.4
C0b	74	18.8	154.2	5.0	6.9
C1	108	28.5	-21.2	15.8	1.0
C2	158	44.3	-23.8	42.8×13.6	0.6
BG	1000	...	...	...	...
eht-imaging (image domain, no blur)					
C0a	228	0.0	...	13.8×12.3	3.1
C0b	86	18.9	154.8	10.3×11.5	1.7
C1	110	35.8	-28.0	13.0×12.7	1.6
BG	978	...	...	...	...

Note. The columns are as follows: (1)—designation of knot; (2)—flux density in mJy; (3)—distance from the core in μas; (4)—position angle with respect to the core in degree; (5)—size in microarcseconds; (6)—observed brightness temperature in 10^{10} K.

show the presence of C2 component, and although uncertainties of the parameters are large, there is a good agreement between the results of Gaussian fits of DIFMAP and eht-imaging modeling.

We have calculated the observed brightness temperature of the knots, $T_{\rm B}$, in the same manner as in Issaoun et al. (2022; no cosmological redshift or Doppler corrections accounted for). According to Table 2, C0 has a higher $T_{\rm B}$ than the C1 component, which supports the interpretation that it is a VLBI core at 1.3 mm. The observed brightness temperature of the core is close to the equipartition value of $T_{\rm eq} \sim 5 \times 10^{10}$ K (Readhead 1994), which implies an intrinsic (plasma frame) brightness temperature $T'_{\rm B} = T_{\rm B}(1+z)/\delta \ll T_{\rm eq}$, if we assume the same Doppler factor of $\delta \sim 9$ on μas scales as estimated on mas scales (Jorstad et al. 2017). A robust comparison with $T_{\rm eq}$ requires calculation of $T_{\rm B}$ either for an optically thin knot or for the flux density corresponding to the

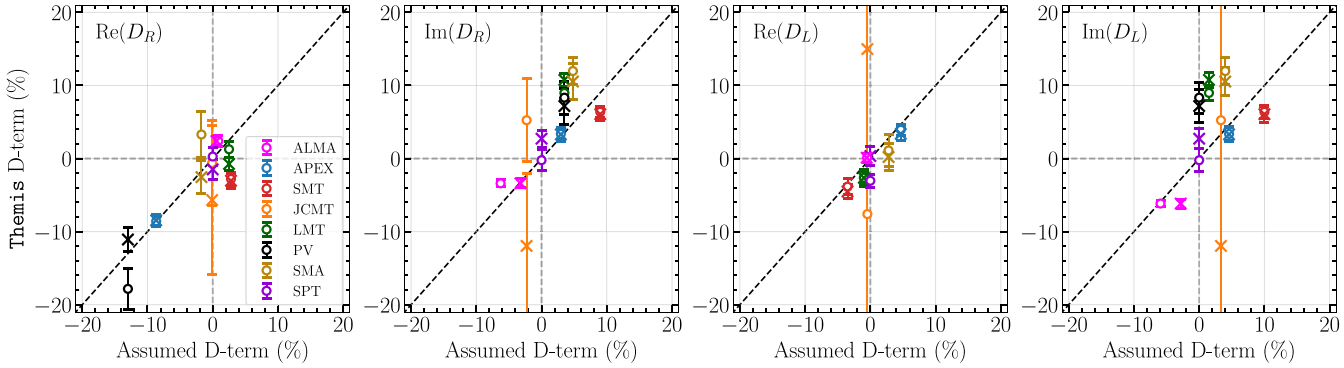

Figure 6. A comparison between the leakage calibration D-terms estimated by Themis from the NRAO 530 data set and D-terms assumed by other imaging methods, following the procedures described in Section 2. Empty circles correspond to the LO band, crosses correspond to the H I band, and error bars represent the 1σ width of the Themis posteriors.

turnover frequency in the spectral energy distribution (SED) of a knot. However, the spectral index obtained for NRAO 530 by Goddi et al. (2021) is steep, $\alpha \sim 0.8$ ($S_\nu \propto \nu^{-\alpha}$), while the source is dominated by the core at 221 GHz, so that even for C0 we can assume that we measure T_B either near the turnover frequency or at the optically thin branch of the SED. The brightness temperature is somewhat higher at lower frequencies, where the core is optically thick. This will be discussed in a separate paper devoted to multiwavelength observations of NRAO 530 (M. M. Lisakov et al. 2023, in preparation). The results shown in Table 2 also contain a large Gaussian component, BG, with a flux density of $\sim$1 Jy, which characterizes the unconstrained source emission on larger angular scales, overresolved on inter-site EHT baselines.

4. Linear Polarization Images

We have performed LP imaging of NRAO 530 using four out of five algorithms described in Section 3: DIFMAP (CLEAN), eht-imaging, DMC, and Themis. SMILI implementation does not currently have the capability to reconstruct polarimetric images. Given the large and poorly constrained systematic uncertainties in the polarimetric calibration of the EHT data at times when ALMA is not participating in observations, only 2017 April 6 and 7 data were used, except for DMC, which allows for a very flexible calibration of complex polarimetric gains simultaneous with the image reconstruction (Pesce 2021), and hence could reliably fit the entire data set. Similarly, except for DMC and Themis, we disregarded JCMT single polarization data for the LP analysis.

4.1. Consistency Test for D-terms

For all methods other than Themis, we either fixed all polarimetric leakage D-terms following the multisource fitting procedures described in EHTC et al. (2021) and Issaoun et al. (2022), or we only solved for the SPT D-terms. The latter resulted in the SPT D-terms being no larger than 1%, with uncertainties comparable to or larger than the values themselves, which justifies setting SPT D-terms to zero. In the case of Themis, we performed full fitting of D-term coefficients simultaneously with the image reconstruction as an additional consistency test. In Figure 6 we provide a comparison between the assumed and estimated D-terms. The results show a generally high level of consistency, particularly when considering the difficulty of quantifying the systematics present in a fit to a single sparsely sampled data set. JCMT D-terms are constrained very poorly as a consequence of the station operating with a single polarization receiver in 2017. There is a good correlation between the assumed and calculated D-terms, corresponding to a Pearson coefficient of 0.86 for the vector of 64 D-terms (ignoring the uncertainties) and median residual of 2% on a single complex D-term. Altogether, the consistency test results support fixing D-terms for the model fitting and data analysis.

4.2. Linear Polarization Images

Figure 7 presents LP images of NRAO 530 in 2017 April, obtained using a selection of methods. The absolute magnitude of LP ($\sqrt{\mathcal{Q}^2 + \mathcal{U}^2}$ for LP Stokes image-domain components $\mathcal{Q}$ and $\mathcal{U}$) is indicated with white contours and the length of the electric vector position angle (EVPA) ticks, while the EVPA tick colors represent fractional LP magnitude. The Faraday rotation toward NRAO 530 is entirely negligible at 230 GHz (Goddi et al. 2021); hence, observed EVPA can be directly interpreted as an intrinsic source property. The grayscale background image and black contours correspond to the total intensity. Similarly as in Section 3.6, in Figure 8 we also present the method-averaged image, where the background image and cyan contours represent the LP magnitude, while the white contours describe the total intensity image map. Similarly as in the case of the total intensity images, we adopted images shown in Figures 7–8 to a common field of view of 128 μas. The contribution of the emission outside of this region is consistent with the image noise.

Figure 8 serves the purpose of identifying the total intensity and LP components. As for the total intensity images, the LP images show similar structure across all algorithms, although there are some differences in the polarization properties of the jet features. The most consistent among the methods is the polarized feature P0 near the core, which has a slight shift to the northeast with respect to the total intensity peak C0 in the DIFMAP, eht-imaging, and DMC images. In the DMC image, the polarized feature in the southeast part of the C1 knot is most prominent, compared to images produced by the other methods. The DIFMAP and DMC images show a polarized feature, P2, associated with the diffuse northeastern total intensity component C2, which has the highest degree of polarization. A hint of this feature can be seen in the eht-imaging image, while the Themis image possesses a prominent polarized feature P1 that is rather a combination of polarization that can be associated with knot C1 and the

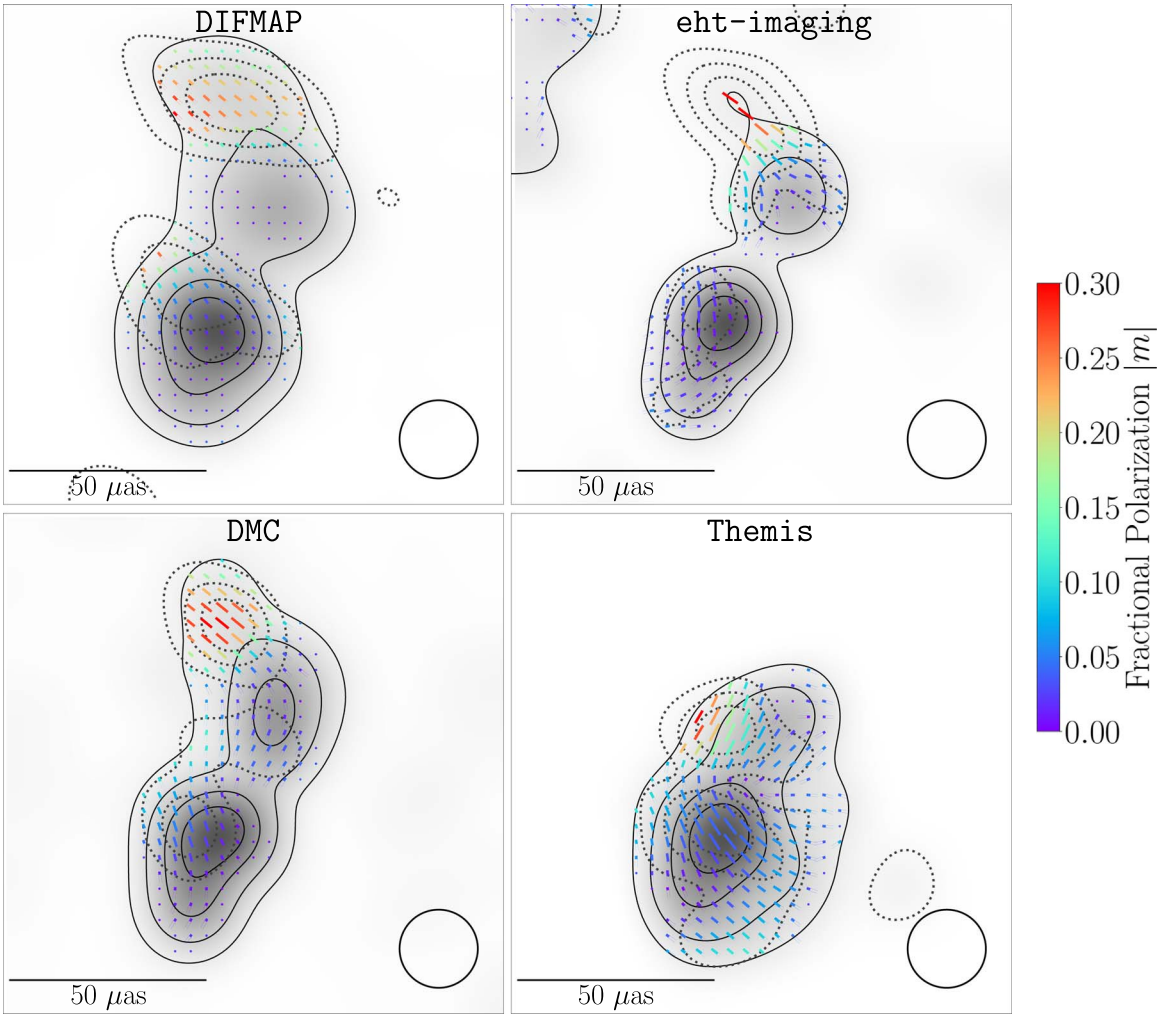

Figure 7. LP images of NRAO 530 produced using `DIFMAP`, `eht-imaging`, `DMC`, and `Themis`. The total intensity is shown in grayscale with black contours indicating 10%, 25%, 50%, and 75% of the peak LP intensity. Black dotted contours indicate 25%, 50%, and 75% of the peak polarized intensity. The ticks show the orientation of the EVPA, their length indicates linearly polarized intensity magnitude, and their color indicates fractional LP. Cuts were made to omit all regions in the images where Stokes $\mathcal{I} < 10\%$ of the peak brightness and $\mathcal{P} < 10\%$ of the peak polarized brightness. The images are all displayed with a field of view of 128 μas, and all images are blurred to an equivalent resolution of 20 μas.

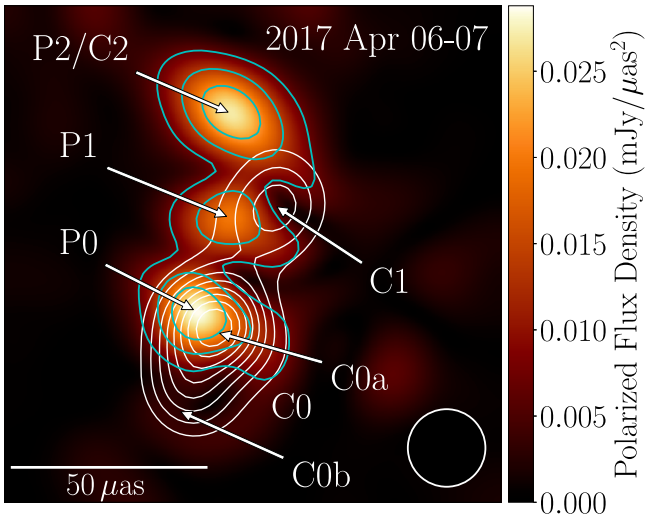

Figure 8. Schematic of the total-intensity (C0, C1, and C2) and LP (P0, P1, and P2) components in the EHT fiducial image of NRAO 530; white contours show the total intensity levels as in Figure 5; color scale and cyan contours represent the polarized intensity of the method-averaged image.

northeastern component. Discrepancies seen in the `Themis` image may be related to the spline raster resolution limitations imposed by the MCMC algorithm. We expect that the method-averaged LP image, shown in Figure 8, should reveal the most reliable image-domain polarization features.

4.3. Linear Polarization Component Modeling

The method-averaged polarized intensity image presented in Figure 8 can be described with three polarized features designated as P0, P1, and P2. Similarly as in Section 3.7, we have modeled Stokes $\mathcal{Q}$ and $\mathcal{U}$ visibilities in `DIFMAP` using the task *modelfit*, in `eht-imaging` Gaussian component geometric modeling framework, and we also used image-domain feature extraction methods to characterize the `eht-imaging` results. Table 3 gives parameters of the polarized components, which are as follows: (1) polarized component; (2) distance between the center of the component and the total intensity peak; (3) position angle of the component with respect to the center; (4) FWHM size of the component; (5) Stokes $\mathcal{Q}$ parameter; (6) Stokes $\mathcal{U}$ parameter; (7) fractional degree of polarization; and (8) component EVPA. Since $\mathcal{Q}$ and $\mathcal{U}$ data were modeled separately in `DIFMAP`, the distance, position

Table 3
Parameters of Polarized Components

Knot (1)	R (μas) (2)	Θ (deg) (3)	a (μas) (4)	Q (mJy) (5)	U (mJy) (6)	m (%) (7)	EVPA (deg) (8)
DIFMAP (Gaussian modeling)							
P0	5.7 ± 2.1	47 ± 32	15.3 ± 0.7	9.8 ± 4.0	14.8 ± 5.0	5.2 ± 1.3	28 ± 7
P1	26.6 ± 1.8	1 ± 9	16.8 ± 1.1	3.0 ± 4.0	-7.7 ± 5.0	6.7 ± 2.5	-34 ± 11
P2	55.8 ± 1.0	6 ± 5	14.0 ± 1.0	-8.4 ± 4.0	13.8 ± 5.0	18.1 ± 4.2	61 ± 12
Map	...	...	...	-6.1 ± 4.0	24.7 ± 5.0	1.7 ± 0.6	52 ± 10
ALMA	...	...	...	-8.6	36.8	2.35 ± 0.03	51.6 ± 0.4
eht-imaging (Gaussian modeling)							
P0	0.0	...	10.6	9.5	10.1	6.6	24.4
P1	28.5	-21	15.8	11.8	-8.8	13.6	-18.4
P2	44.3	-24	42.8×13.6	-6.9	13.0	15.2	59.0
Map	...	...	...	13.6	17.2	4.1	25.8
eht-imaging (image domain, blur 15 μas)							
P0	7.3	68	11.5	7.6	0.5	8.0	2
P1	31.1	12	10.4	5.6	-0.5	22	-3
P2	54.5	7	20.4	-9.8	25.2	58	56
Map	...	...	...	-11.2	15.5	2.7	63

Note. (1) Values presented for the *Map* region are obtained by integrating modes of Stokes $\mathcal{I}$, $\mathcal{Q}$, and $\mathcal{U}$ in the entire VLBI field of view; (2) Parameters presented for ALMA are results obtained by Goddi et al. (2021) on 2017 April 6. The columns are as follows: (1)—designation of knot; (2)—distance from the core in microarcseconds; (3)—position angle with respect to the core in degrees; (4)—size in microarcseconds; (5)—Stokes Q value in millijanskys; (6)—Stokes U value in millijanskys; (7)—degree of polarization in percentage; and (8)—PA of polarization in degrees.

angle, and size of a component are calculated as averages over the $\mathcal{Q}$ and $\mathcal{U}$ values, and standard deviations of the averages are given as uncertainties. The uncertainties in $\mathcal{Q}$ and $\mathcal{U}$ flux intensity are equal to the rms of the $\mathcal{Q}$ and $\mathcal{U}$ map noise. Based on the uncertainties in R, Θ, and a values given in Table 3, there is very good agreement in the position and size of polarized components between $\mathcal{Q}$ and $\mathcal{U}$ images, which supports the robustness of the DIFMAP modeling. We identify polarized components P0, P1, and P2 with the total intensity components C0, C1, and C2, respectively, with parameters of the latter given in Table 2. The distances of the associated total and polarized intensity knots agree within 1.5σ uncertainties, and their sizes are almost identical, except the P2/C2 pair in DIFMAP modeling where the polarized component P2 occupies only a fraction (less than a half) of knot C2. However, the position angles of P0 and P1 show some differences relative to those of C0 and C1, respectively, which cause the centers of the polarized components to be placed at the eastern edge of the corresponding total intensity components. The other EHT Sgr A* calibrator, J1924-2914, does not exhibit a similar effect (Issaoun et al. 2022), despite the fact that the two sources were calibrated in the same way and the same D-terms were employed to correct for the instrumental leakage. Hence, we conclude that these shifts are intrinsic to NRAO 530 rather than caused by instrumental effects.

The LP image in Figure 8 shows polarized component P2, which we associate with total intensity knot C2, detected with Gaussian component models. However, due to its diffuse nature, the surface brightness of the knot is comparable with the noise level, so that C2 is indicated as a marginal feature in Figure 5, yet the knot has the highest degree of polarization in the jet. As mentioned above, in the case of the DIFMAP model polarized emission of C2, knot P2, occupies only a part of the total intensity feature. If we fix the size and position of a total intensity component, C2, equal to those of P2, and search for the total flux density corresponding to the region of P2, this will yield a low value of $\sim$27 mJy, which implies the fractional polarization in the P2 region as high as $\sim$60%. A similarly high degree of polarization is obtained in the case of eht-imaging image-domain analysis. Therefore, the P2 region should have an almost uniform magnetic field, which implies synchrotron emission fractional polarization of $m_{\rm max} = (\alpha + 1)/(\alpha + 5/3) \times 100 = 75\%$ (Pacholczyk 1970), assuming a spectral index for P2 of $\alpha \sim 1$. One of the possible explanations why the knot is prominent in polarization but not in the total intensity is that this feature could be caused by shear, ordering the field, but not by shocks that would make it bright in total intensity. For the geometric modeling of $\mathcal{Q}$ and $\mathcal{U}$ in eht-imaging, we assumed that each total intensity Gaussian component corresponds to an LP component with a constant EVPA and fractional polarization, obtaining a lower fractional polarization of C2/P2, which is nevertheless significantly larger than that of the core component P0.

Image-domain feature extraction with eht-imaging was based on masking disjointed image regions by LP flux density following the procedures used in Issaoun et al. (2022). We obtained three components that could be identified with P0, P1, and P2 from Figure 8. The results given in Table 3 are mostly in qualitative, if not quantitative, agreement between the methods, although the parameters agree within the 1.5σ uncertainties given for values obtained by DIFMAP. The differences that are present can be attributed to the low polarized intensity in the jet relative to the polarized intensity noise and the systematic uncertainties specific to different imaging methods.

Visual inspection of Figure 7 suggests that EVPAs in the P0/C0 region lie between 20° and 35° in all polarization images, except the eht-imaging image, which is also consistent with the result of the $\mathcal{Q}$ and $\mathcal{U}$ map modeling in

DIFMAP and eht-imaging Gaussian modeling. The eht-imaging image shows the EVPA to be closer to 0°, which can be explained by the higher level of polarization noise in the image. All images show polarized emission in the P1 region, with the EVPA close to the jet direction, while the EVPA of P2 is perpendicular to the inner jet position angle as seen in the DIFMAP and DMC images in Figure 7 and determined by modeling.

We have summed all CLEAN modes within the DIFMAP total intensity image in Stokes parameter $\mathcal{I}$ (including the flux density of the BG component; see Table 2), and Stokes parameters $\mathcal{Q}$ and $\mathcal{U}$. This has resulted in an integrated total intensity flux of 1.5 Jy. Polarization parameters integrated over the submilliarcsecond EHT image field of view are listed in Table 3 under the component name "Map." These parameters agree reasonably well with those obtained by Goddi et al. (2021) for NRAO 530 at 221 GHz using ALMA data on 2017 April 6 and 7. There is very little variability of the flux density or polarization parameters between the two days, with flux densities reported by Goddi et al. (2021) equal to 1.61 ± 0.16 Jy (April 6) and 1.57 ± 0.16 Jy (April 7), and polarization parameters obtained on 2017 April 6 reproduced in Table 3 under the component name "ALMA." Including Stokes parameters $\mathcal{Q}$ and $\mathcal{U}$ of the P2 knot in the calculation of Map values is essential for a good agreement with the polarization measurements obtained by Goddi et al. (2021).

4.4. Constraints on Circular Polarization

The circular polarization of NRAO 530 at 230 GHz observed by ALMA (but unresolved) is consistent with zero (Goddi et al. 2021). The high resolution of the EHT observation can be favorable for a detection of the circular polarization in the jet of NRAO 530, which is important for determining the plasma composition (Wardle et al. 1998). To find whether there is a statistically significant signature of spatially resolved circular polarization in the EHT VLBI data, we employed the same procedure as Issaoun et al. (2022), based on exploring the posterior distributions of the DMC fits to the observational data. Using 1000 images drawn from the posterior distribution, and evaluating the mean and standard deviation of circular polarization in each reconstructed pixel, we find no pixel with a Stokes $\mathcal{V}$ detection of significance larger than 1.4σ. Hence, we conclude that we did not find statistically significant circular polarization resolved with the EHT resolution of $\sim$20 μas. For comparison, the same procedure applied to the LP maps confirms detection at the $\sim 7\sigma$ level. Because of large image reconstruction uncertainties, this statement does not translate to a robust upper limit on the fractional circular polarization.

5. Discussion

The high-resolution total and polarized intensity images of the quasar NRAO 530 at 230 GHz obtained during the EHT campaign in 2017 April indicate a jet direction of $\sim -28°$ on μas scales. This jet direction is different from those seen at 86 GHz (PA $\sim 10°$; Issaoun et al. 2019) and 43 GHz (PA $\sim -3°$; Weaver et al. 2022), implying a wiggling of the jet with the distance from the core. In fact, the PA of component C2/P2 (see Table 3) agrees with that of the jet direction at 86 GHz within the uncertainties, which can be a sign of jet curvature already at this location. If that is indeed the case, the EVPA of the P2 component could be more aligned with the local direction of the bending jet, which supports the origin of the emission in the shear. The curvature could be caused by an imbalance between the pressure inside and outside the jet resulting in the development of instabilities in the flow, or it could be connected with jet precession. An analysis of the jet structure from subparsec to kiloparsec scales using multiwavelength VLBI images of NRAO 530 contemporaneous with the 230 GHz EHT image will be presented in Lisakov et al. (2023, in preparation).

The brightest feature in the source, C0, which we associate with the VLBI core at 1.3 mm, is complex and consists of two components, C0a and C0b. Complex structure in the core was also revealed in the EHT images of the quasar 3C 279 (Kim et al. 2020). Variability of such core structures can be expected on short timescales with quasiperiodic oscillations produced by kink instabilities in the case of a magnetically dominated jet (Dong et al. 2020). The intrinsic brightness temperatures of both C0 components are lower than the equipartition brightness temperature (see Table 2), even if the Doppler factor of the jet on microarcsecond scales is lower than that found on milliarcsecond scales. A possible explanation is that the energy density of the jet on microarcsecond scales is dominated by the magnetic field.

Homan et al. (2006) analyzed the brightness temperatures of VLBI cores at 15 GHz of a large sample of AGNs. They found that, in a quiescent state, cores have a narrow range of intrinsic brightness temperatures close to the value expected for equipartition, while during outbursts the characteristic intrinsic brightness temperature significantly exceeds $T_{\rm eq}$. The authors have estimated that in active states, the energy in radiating particles exceeds the energy in the magnetic field by a factor of $\sim 10^5$. This implies that somewhere between the 230 and 15 GHz cores, there is a region where a magnetically dominated jet changes its state and reaches equipartition conditions. Moreover, Jorstad et al. (2007) suggested, based on quasi-simultaneous multiepoch observations at 43 GHz (VLBA), 86 GHz (BIMA[157]), and 230/345 GHz (JCMT), that this region is located between the 86 and 43 GHz VLBI cores, while Lee (2013) found that 86 GHz VLBI cores in a sample of compact radio sources observed with Global Millimeter VLBI Array have a characteristic intrinsic brightness temperature lower than the equipartition temperature. The observed low brightness temperature of C0 somewhat supports this scenario. However, analysis of the simultaneous VLBI observations at 230 and 86 GHz is needed to draw firm conclusions.

The polarized features in the jet are shifted with respect to the total intensity components with which they are associated. The shifts are almost transverse to the inner jet direction—the jet direction is from southeast to northwest, while the shifts are to the east. This feature appears robust in the image reconstructions. One viable interpretation of this phenomenon involves a difference in ordering of the magnetic field transverse to the jet, with the magnetic field on the eastern part of the jet being more ordered than that of the western part. This can be understood if the magnetic field in the jet consists of two components—ordered and turbulent, with the turbulent component being more pronounced on the western side of the jet, while a helical magnetic field can represent the ordered component. Indeed, a helical structure of the magnetic field is supported by the EVPA behavior in different polarized

[157] The Berkeley–Illinois–Maryland Array- Association (BIMA) operated at 3 mm and 1.3 mm until 2004.

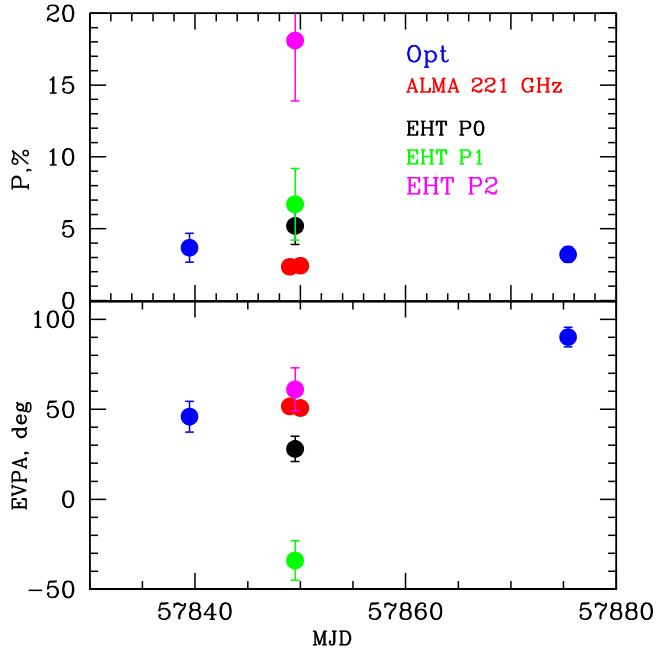

Figure 9. Top: degree of LP at the optical *R* band (blue), ALMA at 221 GHz (red), and EHT knots P0 (black), P1 (green), and P2 (magenta). Bottom: PA of polarization with the same color coding; parameters of knots are shown according to the DIFMAP model.

components. The EVPA undergoes significant changes along ∼60 μas of the jet length: it goes from being oblique in the core to aligning with the jet direction in P1 ∼30 μas to perpendicular to the inner jet direction in P2 ∼55 μas from the core. In addition, a higher polarization at the western side can be attributed to velocity shear between the jet boundary and the ambient medium being stronger on the western side, which is consistent with the explanation of the nature of component P2/C2. However, the EVPA behavior is more aligned with a helical magnetic field, although we do not have a sufficient resolution to resolve the EVPA structure across the jet. Recent work by Pushkarev et al. (2022) analyzed the polarization properties in a large sample of AGNs observed with the VLBA at 15 GHz within the MOJAVE survey, which presented transverse fractional polarization slices beyond the core region for 307 sources. The authors have found that the majority of the sources (including NRAO 530) show a clear increase in fractional polarization toward the jet edges, with an asymmetric profile. They suggest that the observed patterns of polarization can be explained by helical magnetic fields with different pitch angles and different geometric and kinematic parameters of the jet, which is surrounded by a sheath. It therefore appears that a helical magnetic field structure persists in the quasar jet from subparsec to hundred-parsec scales.

In addition to EHT data, we have obtained optical polarization observations of NRAO 530 several days before and after the EHT campaign. Figure 9 shows polarization measurements in the optical *R* band, at 221 GHz for the arcsecond resolution of ALMA (Goddi et al. 2021), and those of the EHT resolved components at 230 GHz. The optical observations were carried out with the 1.8 m Perkins telescope (Flagstaff, AZ) using the PRISM camera. The description of data reduction can be found in Jorstad et al. (2010). When comparing to the optical and ALMA values, the best agreement across wavelengths is found with the P2 component, indicating dominance of the magnetic field direction perpendicular to the microarcsecond scale jet direction in the source. This suggests that the magnetic field direction in the optical emission region is similar to that of P2, which has the highest degree of polarization in the jet.

6. Summary

Using the 2017 EHT observations, we have obtained the first total and polarized intensity images of the quasar NRAO 530 at 230 GHz, with an unprecedented angular resolution of ∼20 μas. We have not detected statistically significant variability of the source structure on a timescale of 3 days, and hence we have combined the data over epochs and frequencies to generate final images. We have used a variety of methods to construct the total and linearly polarized intensity images and averaged the final reconstructions produced by different methods to obtain the fiducial total and polarized intensity maps.

On microarcsecond scales, the quasar has a bright core of ∼300 mJy, with a jet extending up to 60 μas along a PA ∼ −28°. The core has substructure consisting of two features, C0a and C0b. We associate the 1.3 mm VLBI core with the brightest knot, C0a, while C0b, located at a PA ∼ +155° and ∼3 times weaker than C0a can be a more opaque region of the core. The core is polarized, with a degree of polarization of ∼5%−8%. The extended jet includes two features, C1/P1 and C2/P2, with mutually orthogonal directions of polarization, parallel and perpendicular to the jet, respectively, suggestive of a helical magnetic field structure. The centers of the polarized knots P0 and P1 are shifted slightly transverse to the jet with respect to the centers of the corresponding total intensity knots C0 and C1. This can be caused either by a more ordered magnetic field on the eastern side of the jet, connected with a helical structure of the magnetic field, or a stronger interaction between the jet and the external medium on this side.

Feature C2 has the highest degree of polarization in the jet, ∼20%. However, polarized knot P2, which occupies only a fraction of the total area of C2, has a peak polarization of ∼60%. The latter implies a nearly uniform magnetic field in the P2 region. In fact, the optical polarization measurement nearest in time to the EHT campaign has an EVPA similar to that in P2. NRAO 530 is a bright γ-ray source, and the origin of high-energy emission in blazars continues to be highly debated. We can speculate that the P2 region, with a very uniform magnetic field, might be a location where nonthermal optical and high-energy emission originates. Future multiepoch and multi-wavelength observations of the source simultaneous with EHT campaigns can provide a significant advance toward understanding the location of the high-energy dissipation zone in blazar jets.

The Event Horizon Telescope Collaboration thanks the following organizations and programs: the Academia Sinica; the Academy of Finland (projects 274477, 284495, 312496, 315721); the Agencia Nacional de Investigación y Desarrollo (ANID), Chile via NCN19_058 (TITANs) and Fondecyt 1221421, the Alexander von Humboldt Stiftung; an Alfred P. Sloan Research Fellowship; Allegro, the European ALMA Regional Centre node in the Netherlands, the NL astronomy research network NOVA and the astronomy institutes of the University of Amsterdam, Leiden University and Radboud

University; the ALMA North America Development Fund; the black hole Initiative, which is funded by grants from the John Templeton Foundation and the Gordon and Betty Moore Foundation (although the opinions expressed in this work are those of the author(s) and do not necessarily reflect the views of these Foundations); Chandra DD7-18089X and TM6-17006X; the China Scholarship Council; China Postdoctoral Science Foundation fellowship (2020M671266); Consejo Nacional de Ciencia y Tecnología (CONACYT, Mexico, projects U0004-246083, U0004-259839, F0003-272050, M0037-279006, F0003-281692, 104497, 275201, 263356); the Consejería de Economía, Conocimiento, Empresas y Universidad of the Junta de Andalucía (grant P18-FR-1769), the Consejo Superior de Investigaciones Científicas (grant 2019AEP112); the Delaney Family via the Delaney Family John A. Wheeler Chair at Perimeter Institute; Dirección General de Asuntos del Personal Académico-Universidad Nacional Autónoma de México (DGAPA-UNAM, projects IN112417 and IN112820); the Dutch Organization for Scientific Research (NWO) VICI award (grant 639.043.513) and grant OCENW.KLEIN.113; the Dutch National Supercomputers, Cartesius and Snellius (NWO Grant 2021.013); the EACOA Fellowship awarded by the East Asia Core Observatories Association, which consists of the Academia Sinica Institute of Astronomy and Astrophysics, the National Astronomical Observatory of Japan, Center for Astronomical Mega-Science, Chinese Academy of Sciences, and the Korea Astronomy and Space Science Institute; the European Research Council (ERC) Synergy Grant "BlackHoleCam: Imaging the Event Horizon of Black Holes" (grant 610058); the European Union Horizon 2020 research and innovation program under grant agreements RadioNet (No. 730562) and M2FINDERS (No. 101018682); the Horizon ERC Grants 2021 program under grant agreement No. 101040021; the Generalitat Valenciana postdoctoral grant APOSTD/2018/177 and GenT Program (project CIDEGENT/2018/021); MICINN Research Project PID2019-108995GB-C22; the European Research Council for advanced grant "JETSET: Launching, propagation and emission of relativistic jets from binary mergers and across mass scales" (grant No. 884631); the Institute for Advanced Study; the Istituto Nazionale di Fisica Nucleare (INFN) sezione di Napoli, iniziative specifiche TEONGRAV; the International Max Planck Research School for Astronomy and Astrophysics at the Universities of Bonn and Cologne; DFG research grant "Jet physics on horizon scales and beyond" (grant No. FR 4069/2-1); Joint Columbia/Flatiron Postdoctoral Fellowship, research at the Flatiron Institute is supported by the Simons Foundation; the Japan Ministry of Education, Culture, Sports, Science and Technology (MEXT; grant JPMXP1020200109); the Japanese Government (Monbukagakusho: MEXT) Scholarship; the Japan Society for the Promotion of Science (JSPS) Grant-in-Aid for JSPS Research Fellowship (JP17J08829); the Joint Institute for Computational Fundamental Science, Japan; the Key Research Program of Frontier Sciences, Chinese Academy of Sciences (CAS, grants QYZDJ-SSW-SLH057, QYZDJS SW-SYS008, ZDBS-LY-SLH011); the Leverhulme Trust Early Career Research Fellowship; the Max-Planck-Gesell schaft (MPG); the Max Planck Partner Group of the MPG and the CAS; the MEXT/JSPS KAKENHI (grants 18KK0090, JP21H01137, JP18H03721, JP18K13594, 18K03709, JP19K1 4761, 18H01245, 25120007); the Malaysian Fundamental Research Grant Scheme (FRGS) FRGS/1/2019/STG02/UM/02/6; the MIT International Science and Technology Initiatives (MISTI) Funds; the Ministry of Science and Technology (MOST) of Taiwan (103-2119-M-001-010-MY2, 105-2112-M-001-025-MY3, 105-2119-M-001-042, 106-2112-M-001-011, 106-2119-M-001-013, 106-2119-M-001-027, 106-2923-M-001-005, 107-2119-M-001-017, 107-2119-M-001-020, 107-2119-M-001-041, 107-2119-M-110-005, 107-2923-M-001-009, 108-2112-M-001-048, 108-2112-M-001-051, 108-2923-M-001-002, 109-2112-M-001-025, 109-2124-M-001-005, 109-2923-M-001-001, 110-2112-M-003-007-MY2, 110-2112-M-001-033, 110-2124-M-001-007, and 110-2923-M-001-001); the Ministry of Education (MoE) of Taiwan Yushan Young Scholar Program; the Physics Division, National Center for Theoretical Sciences of Taiwan; the National Aeronautics and Space Administration (NASA, Fermi Guest Investigator grants 80NSSC20K1567 and 80NSSC22K1571, NASA Astrophysics Theory Program grant 80NSSC20K0527, NASA NuSTAR award 80NSSC20K0645); NASA Hubble Fellowship grants HST-HF2-51431.001-A, HST-HF2-51482.001-A awarded by the Space Telescope Science Institute, which is operated by the Association of Universities for Research in Astronomy, Inc., for NASA, under contract NAS5-26555; the National Institute of Natural Sciences (NINS) of Japan; the National Key Research and Development Program of China (grant 2016YFA0400704, 2017YFA0402703, 2016YFA040 0702); the National Science Foundation (NSF, grants AST-0096454, AST-0352953, AST-0521233, AST-0705062, AST-0905844, AST-0922984, AST-1126433, AST-1140030, DGE-1144085, AST-1207704, AST-1207730, AST-1207752, MRI-1228509, OPP-1248097, AST-1310896, AST-1440254, AST-1555365, AST-1614868, AST-1615796, AST-1715061, AST-1716327, AST-1716536, OISE-1743747, AST-1816420, AST-1935980, AST-2034306); NSF Astronomy and Astrophysics Postdoctoral Fellowship (AST-1903847); the Natural Science Foundation of China (grants 11650110427, 10625314, 11721303, 11725312, 11873028, 11933007, 11991052, 119910 53, 12192220, 12192223); the Natural Sciences and Engineering Research Council of Canada (NSERC, including a Discovery grant and the NSERC Alexander Graham Bell Canada Graduate Scholarships-Doctoral Program); the National Youth Thousand Talents Program of China; the National Research Foundation of Korea (the Global PhD Fellowship grant: grants NRF-2015H1A2A1033752, the Korea Research Fellowship Program: NRF-2015H1D3A1066561, Brain Pool Program: 2019H1D3A1A01102564, Basic Research Support grant 2019R1F1A1059721, 2021R1A6A3A01086420, 2022R1C1C1005255); Netherlands Research School for Astronomy (NOVA) Virtual Institute of Accretion (VIA) postdoctoral fellowships; Onsala Space Observatory (OSO) national infrastructure, for the provisioning of its facilities/observational support (OSO receives funding through the Swedish Research Council under grant 2017-00648); the Perimeter Institute for Theoretical Physics (research at Perimeter Institute is supported by the Government of Canada through the Department of Innovation, Science and Economic Development and by the Province of Ontario through the Ministry of Research, Innovation and Science); the Princeton Gravity Initiative; the Spanish Ministerio de Ciencia e Innovación (grants PGC2018-098915-B-C21, AYA2016-80889-P, PID 2019-108995GB-C21, PID2020-117404GB-C21); the University of Pretoria for financial aid in the provision of the new Cluster Server nodes and SuperMicro (USA) for a SEEDING

grant approved toward these nodes in 2020; the Shanghai Pilot Program for Basic Research, Chinese Academy of Science, Shanghai Branch (JCYJ-SHFY-2021-013); the State Agency for Research of the Spanish MCIU through the "Center of Excellence Severo Ochoa" award for the Instituto de Astrofísica de Andalucía (SEV-2017-0709); the Spinoza Prize SPI 78-409; the South African Research Chairs Initiative, through the South African Radio Astronomy Observatory (SARAO, grant ID 77948), which is a facility of the National Research Foundation (NRF), an agency of the Department of Science and Innovation (DSI) of South Africa; the Toray Science Foundation; the Swedish Research Council (VR); the US Department of Energy (USDOE) through the Los Alamos National Laboratory (operated by Triad National Security, LLC, for the National Nuclear Security Administration of the USDOE (Contract 89233218CNA000001); and the YCAA Prize Postdoctoral Fellowship.

We thank the staff at the participating observatories, correlation centers, and institutions for their enthusiastic support. This paper makes use of the following ALMA data: ADS/JAO.ALMA#2016.1.01154.V. ALMA is a partnership of the European Southern Observatory (ESO; Europe, representing its member states), NSF, and National Institutes of Natural Sciences of Japan, together with National Research Council (Canada), Ministry of Science and Technology (MOST; Taiwan), Academia Sinica Institute of Astronomy and Astrophysics (ASIAA; Taiwan), and Korea Astronomy and Space Science Institute (KASI; Republic of Korea), in cooperation with the Republic of Chile. The Joint ALMA Observatory is operated by ESO, Associated Universities, Inc. (AUI)/NRAO, and the National Astronomical Observatory of Japan (NAOJ). The NRAO is a facility of the NSF operated under cooperative agreement by AUI. This research used resources of the Oak Ridge Leadership Computing Facility at the Oak Ridge National Laboratory, which is supported by the Office of Science of the U.S. Department of Energy under contract No. DE-AC05-00OR22725. We also thank the Center for Computational Astrophysics, National Astronomical Observatory of Japan. The computing cluster of Shanghai VLBI correlator supported by the Special Fund for Astronomy from the Ministry of Finance in China is acknowledged. This work was supported by FAPESP (Fundacao de Amparo a Pesquisa do Estado de Sao Paulo) under grant 2021/01183-8.

APEX is a collaboration between the Max-Planck-Institut für Radioastronomie (Germany), ESO, and the Onsala Space Observatory (Sweden). The SMA is a joint project between the SAO and ASIAA and is funded by the Smithsonian Institution and the Academia Sinica. The JCMT is operated by the East Asian Observatory on behalf of the NAOJ, ASIAA, and KASI, as well as the Ministry of Finance of China, Chinese Academy of Sciences, and the National Key Research and Development Program (No. 2017YFA0402700) of China and Natural Science Foundation of China grant 11873028. Additional funding support for the JCMT is provided by the Science and Technologies Facility Council (UK) and participating universities in the UK and Canada. The LMT is a project operated by the Instituto Nacional de Astrófisica, Óptica, y Electrónica (Mexico) and the University of Massachusetts at Amherst (USA). The IRAM 30 m telescope on Pico Veleta, Spain is operated by IRAM and supported by CNRS (Centre National de la Recherche Scientifique, France), MPG (Max-Planck-Gesellschaft, Germany) and IGN (Instituto Geográfico Nacional, Spain). The SMT is operated by the Arizona Radio Observatory, a part of the Steward Observatory of the University of Arizona, with financial support of operations from the State of Arizona and financial support for instrumentation development from the NSF. Support for SPT participation in the EHT is provided by the National Science Foundation through award OPP-1852617 to the University of Chicago. Partial support is also provided by the Kavli Institute of Cosmological Physics at the University of Chicago. The SPT hydrogen maser was provided on loan from the GLT, courtesy of ASIAA.

This work used the Extreme Science and Engineering Discovery Environment (XSEDE), supported by NSF grant ACI-1548562, and CyVerse, supported by NSF grants DBI-0735191, DBI-1265383, and DBI-1743442. XSEDE Stampede2 resource at TACC was allocated through TG-AST170024 and TG-AST080026N. XSEDE JetStream resource at PTI and TACC was allocated through AST170028. This research is part of the Frontera computing project at the Texas Advanced Computing Center through the Frontera Large-Scale Community Partnerships allocation AST20023. Frontera is made possible by National Science Foundation award OAC-1818253. This research was carried out using resources provided by the Open Science Grid, which is supported by the National Science Foundation and the U.S. Department of Energy Office of Science. Additional work used ABACUS2.0, which is part of the eScience center at Southern Denmark University. Simulations were also performed on the SuperMUC cluster at the LRZ in Garching, on the LOEWE cluster in CSC in Frankfurt, on the HazelHen cluster at the HLRS in Stuttgart, and on the Pi2.0 and Siyuan Mark-I at Shanghai Jiao Tong University. The computer resources of the Finnish IT Center for Science (CSC) and the Finnish Computing Competence Infrastructure (FCCI) project are acknowledged. This research was enabled in part by support provided by Compute Ontario (http://computeontario.ca), Calcul Quebec (http://www.calculquebec.ca), and Compute Canada (http://www.computecanada.ca).

The EHTC has received generous donations of FPGA chips from Xilinx Inc., under the Xilinx University Program. The EHTC has benefited from technology shared under open-source license by the Collaboration for Astronomy Signal Processing and Electronics Research (CASPER). The EHT project is grateful to T4Science and Microsemi for their assistance with Hydrogen Masers. This research has made use of NASA's Astrophysics Data System. We gratefully acknowledge the support provided by the extended staff of the ALMA, both from the inception of the ALMA Phasing Project through the observational campaigns of 2017 and 2018. We would like to thank A. Deller and W. Brisken for EHT-specific support with the use of DiFX. We thank Martin Shepherd for the addition of extra features in the Difmap software that were used for the CLEAN imaging results presented in this paper. We acknowledge the significance and cultural reverance that Maunakea, where the SMA and JCMT EHT stations are located, has always held within the indigenous Hawaiian people.

Software: `DIFMAP` (Shepherd 1997), `Matplotlib` (Hunter 2007), `DiFX` (Deller et al. 2011), `NumPy` (van der Walt et al. 2011), `eht-imaging` (Chael et al. 2016), `PolConvert` (Martí-Vidal et al. 2016), `SMILI` (Akiyama et al. 2017), `EHT-HOPS` (Blackburn et al. 2019), `Themis` (Broderick et al. 2020a), `DMC` (Pesce 2021).

ORCID iDs

Svetlana Jorstad https://orcid.org/0000-0001-6158-1708
Maciek Wielgus https://orcid.org/0000-0002-8635-4242
Rocco Lico https://orcid.org/0000-0001-7361-2460
Sara Issaoun https://orcid.org/0000-0002-5297-921X
Avery E. Broderick https://orcid.org/0000-0002-3351-760X
Dominic W. Pesce https://orcid.org/0000-0002-5278-9221
Jun Liu (刘俊) https://orcid.org/0000-0002-7615-7499
Guang-Yao Zhao https://orcid.org/0000-0002-4417-1659
Thomas P. Krichbaum https://orcid.org/0000-0002-4892-9586
Lindy Blackburn https://orcid.org/0000-0002-9030-642X
Chi-kwan Chan https://orcid.org/0000-0001-6337-6126
Michael Janssen https://orcid.org/0000-0001-8685-6544
Venkatessh Ramakrishnan https://orcid.org/0000-0002-9248-086X
Kazunori Akiyama https://orcid.org/0000-0002-9475-4254
Antxon Alberdi https://orcid.org/0000-0002-9371-1033
Juan Carlos Algaba https://orcid.org/0000-0001-6993-1696
Katherine L. Bouman https://orcid.org/0000-0003-0077-4367
Ilje Cho https://orcid.org/0000-0001-6083-7521
Antonio Fuentes https://orcid.org/0000-0002-8773-4933
José L. Gómez https://orcid.org/0000-0003-4190-7613
Mark Gurwell https://orcid.org/0000-0003-0685-3621
Michael D. Johnson https://orcid.org/0000-0002-4120-3029
Jae-Young Kim https://orcid.org/0000-0001-8229-7183
Ru-Sen Lu (路如森) https://orcid.org/0000-0002-7692-7967
Iván Martí-Vidal https://orcid.org/0000-0003-3708-9611
Monika Moscibrodzka https://orcid.org/0000-0002-4661-6332
Felix M. Pötzl https://orcid.org/0000-0002-6579-8311
Efthalia Traianou https://orcid.org/0000-0002-1209-6500
Ilse van Bemmel https://orcid.org/0000-0001-5473-2950
Richard Anantua https://orcid.org/0000-0003-3457-7660
Keiichi Asada https://orcid.org/0000-0001-6988-8763
Rebecca Azulay https://orcid.org/0000-0002-2200-5393
Uwe Bach https://orcid.org/0000-0002-7722-8412
Anne-Kathrin Baczko https://orcid.org/0000-0003-3090-3975
Mislav Baloković https://orcid.org/0000-0003-0476-6647
John Barrett https://orcid.org/0000-0002-9290-0764
Michi Bauböck https://orcid.org/0000-0002-5518-2812
Bradford A. Benson https://orcid.org/0000-0002-5108-6823
Raymond Blundell https://orcid.org/0000-0002-5929-5857
Geoffrey C. Bower https://orcid.org/0000-0003-4056-9982
Hope Boyce https://orcid.org/0000-0002-6530-5783
Christiaan D. Brinkerink https://orcid.org/0000-0002-2322-0749
Roger Brissenden https://orcid.org/0000-0002-2556-0894
Silke Britzen https://orcid.org/0000-0001-9240-6734
Dominique Broguiere https://orcid.org/0000-0001-9151-6683
Thomas Bronzwaer https://orcid.org/0000-0003-1151-3971
Sandra Bustamante https://orcid.org/0000-0001-6169-1894
Do-Young Byun https://orcid.org/0000-0003-1157-4109
John E. Carlstrom https://orcid.org/0000-0002-2044-7665
Chiara Ceccobello https://orcid.org/0000-0002-4767-9925
Andrew Chael https://orcid.org/0000-0003-2966-6220
Koushik Chatterjee https://orcid.org/0000-0002-2825-3590
Shami Chatterjee https://orcid.org/0000-0002-2878-1502
Ming-Tang Chen https://orcid.org/0000-0001-6573-3318
Yongjun Chen (陈永军) https://orcid.org/0000-0001-5650-6770
Xiaopeng Cheng https://orcid.org/0000-0003-4407-9868
Pierre Christian https://orcid.org/0000-0001-6820-9941
Nicholas S. Conroy https://orcid.org/0000-0003-2886-2377
John E. Conway https://orcid.org/0000-0003-2448-9181
James M. Cordes https://orcid.org/0000-0002-4049-1882
Thomas M. Crawford https://orcid.org/0000-0001-9000-5013
Geoffrey B. Crew https://orcid.org/0000-0002-2079-3189
Alejandro Cruz-Osorio https://orcid.org/0000-0002-3945-6342
Yuzhu Cui (崔玉竹) https://orcid.org/0000-0001-6311-4345
Jordy Davelaar https://orcid.org/0000-0002-2685-2434
Mariafelicia De Laurentis https://orcid.org/0000-0002-9945-682X
Roger Deane https://orcid.org/0000-0003-1027-5043
Jessica Dempsey https://orcid.org/0000-0003-1269-9667
Gregory Desvignes https://orcid.org/0000-0003-3922-4055
Jason Dexter https://orcid.org/0000-0003-3903-0373
Vedant Dhruv https://orcid.org/0000-0001-6765-877X
Sheperd S. Doeleman https://orcid.org/0000-0002-9031-0904
Sean Dougal https://orcid.org/0000-0002-3769-1314
Sergio A. Dzib https://orcid.org/0000-0001-6010-6200
Ralph P. Eatough https://orcid.org/0000-0001-6196-4135
Razieh Emami https://orcid.org/0000-0002-2791-5011
Heino Falcke https://orcid.org/0000-0002-2526-6724
Joseph Farah https://orcid.org/0000-0003-4914-5625
Vincent L. Fish https://orcid.org/0000-0002-7128-9345
Ed Fomalont https://orcid.org/0000-0002-9036-2747
H. Alyson Ford https://orcid.org/0000-0002-9797-0972
Raquel Fraga-Encinas https://orcid.org/0000-0002-5222-1361
Per Friberg https://orcid.org/0000-0002-8010-8454
Christian M. Fromm https://orcid.org/0000-0002-1827-1656
Peter Galison https://orcid.org/0000-0002-6429-3872
Charles F. Gammie https://orcid.org/0000-0001-7451-8935
Roberto García https://orcid.org/0000-0002-6584-7443
Olivier Gentaz https://orcid.org/0000-0002-0115-4605
Boris Georgiev https://orcid.org/0000-0002-3586-6424
Ciriaco Goddi https://orcid.org/0000-0002-2542-7743
Roman Gold https://orcid.org/0000-0003-2492-1966
Arturo I. Gómez-Ruiz https://orcid.org/0000-0001-9395-1670
Minfeng Gu (顾敏峰) https://orcid.org/0000-0002-4455-6946
Kazuhiro Hada https://orcid.org/0000-0001-6906-772X
Daryl Haggard https://orcid.org/0000-0001-6803-2138
Michael H. Hecht https://orcid.org/0000-0002-4114-4583
Ronald Hesper https://orcid.org/0000-0003-1918-6098
Dirk Heumann https://orcid.org/0000-0002-7671-0047
Luis C. Ho (何子山) https://orcid.org/0000-0001-6947-5846
Paul Ho https://orcid.org/0000-0002-3412-4306
Mareki Honma https://orcid.org/0000-0003-4058-9000
Chih-Wei L. Huang https://orcid.org/0000-0001-5641-3953
Lei Huang (黄磊) https://orcid.org/0000-0002-1923-227X
Shiro Ikeda https://orcid.org/0000-0002-2462-1448
C. M. Violette Impellizzeri https://orcid.org/0000-0002-3443-2472
Makoto Inoue https://orcid.org/0000-0001-5037-3989
David J. James https://orcid.org/0000-0001-5160-4486

Buell T. Jannuzi https://orcid.org/0000-0002-1578-6582
Britton Jeter https://orcid.org/0000-0003-2847-1712
Wu Jiang (江悟) https://orcid.org/0000-0001-7369-3539
Alejandra Jiménez-Rosales https://orcid.org/0000-0002-2662-3754
Abhishek V. Joshi https://orcid.org/0000-0002-2514-5965
Taehyun Jung https://orcid.org/0000-0001-7003-8643
Mansour Karami https://orcid.org/0000-0001-7387-9333
Ramesh Karuppusamy https://orcid.org/0000-0002-5307-2919
Tomohisa Kawashima https://orcid.org/0000-0001-8527-0496
Garrett K. Keating https://orcid.org/0000-0002-3490-146X
Mark Kettenis https://orcid.org/0000-0002-6156-5617
Dong-Jin Kim https://orcid.org/0000-0002-7038-2118
Jongsoo Kim https://orcid.org/0000-0002-1229-0426
Junhan Kim https://orcid.org/0000-0002-4274-9373
Motoki Kino https://orcid.org/0000-0002-2709-7338
Jun Yi Koay https://orcid.org/0000-0002-7029-6658
Prashant Kocherlakota https://orcid.org/0000-0001-7386-7439
Shoko Koyama https://orcid.org/0000-0002-3723-3372
Carsten Kramer https://orcid.org/0000-0002-4908-4925
Michael Kramer https://orcid.org/0000-0002-4175-2271
Cheng-Yu Kuo https://orcid.org/0000-0001-6211-5581
Noemi La Bella https://orcid.org/0000-0002-8116-9427
Tod R. Lauer https://orcid.org/0000-0003-3234-7247
Daeyoung Lee https://orcid.org/0000-0002-3350-5588
Sang-Sung Lee https://orcid.org/0000-0002-6269-594X
Po Kin Leung https://orcid.org/0000-0002-8802-8256
Aviad Levis https://orcid.org/0000-0001-7307-632X
Zhiyuan Li (李志远) https://orcid.org/0000-0003-0355-6437
Greg Lindahl https://orcid.org/0000-0002-6100-4772
Michael Lindqvist https://orcid.org/0000-0002-3669-0715
Mikhail Lisakov https://orcid.org/0000-0001-6088-3819
Kuo Liu https://orcid.org/0000-0002-2953-7376
Elisabetta Liuzzo https://orcid.org/0000-0003-0995-5201
Wen-Ping Lo https://orcid.org/0000-0003-1869-2503
Andrei P. Lobanov https://orcid.org/0000-0003-1622-1484
Laurent Loinard https://orcid.org/0000-0002-5635-3345
Colin J. Lonsdale https://orcid.org/0000-0003-4062-4654
Nicholas R. MacDonald https://orcid.org/0000-0002-6684-8691
Jirong Mao (毛基荣) https://orcid.org/0000-0002-7077-7195
Nicola Marchili https://orcid.org/0000-0002-5523-7588
Sera Markoff https://orcid.org/0000-0001-9564-0876
Daniel P. Marrone https://orcid.org/0000-0002-2367-1080
Alan P. Marscher https://orcid.org/0000-0001-7396-3332
Satoki Matsushita https://orcid.org/0000-0002-2127-7880
Lynn D. Matthews https://orcid.org/0000-0002-3728-8082
Lia Medeiros https://orcid.org/0000-0003-2342-6728
Karl M. Menten https://orcid.org/0000-0001-6459-0669
Daniel Michalik https://orcid.org/0000-0002-7618-6556
Izumi Mizuno https://orcid.org/0000-0002-7210-6264
Yosuke Mizuno https://orcid.org/0000-0002-8131-6730
James M. Moran https://orcid.org/0000-0002-3882-4414
Kotaro Moriyama https://orcid.org/0000-0003-1364-3761
Cornelia Müller https://orcid.org/0000-0002-2739-2994
Alejandro Mus https://orcid.org/0000-0003-0329-6874
Gibwa Musoke https://orcid.org/0000-0003-1984-189X
Ioannis Myserlis https://orcid.org/0000-0003-3025-9497
Andrew Nadolski https://orcid.org/0000-0001-9479-9957
Hiroshi Nagai https://orcid.org/0000-0003-0292-3645
Neil M. Nagar https://orcid.org/0000-0001-6920-662X
Masanori Nakamura https://orcid.org/0000-0001-6081-2420
Ramesh Narayan https://orcid.org/0000-0002-1919-2730
Gopal Narayanan https://orcid.org/0000-0002-4723-6569
Iniyan Natarajan https://orcid.org/0000-0001-8242-4373
Joey Neilsen https://orcid.org/0000-0002-8247-786X
Roberto Neri https://orcid.org/0000-0002-7176-4046
Chunchong Ni https://orcid.org/0000-0003-1361-5699
Aristeidis Noutsos https://orcid.org/0000-0002-4151-3860
Michael A. Nowak https://orcid.org/0000-0001-6923-1315
Junghwan Oh https://orcid.org/0000-0002-4991-9638
Hiroki Okino https://orcid.org/0000-0003-3779-2016
Héctor Olivares https://orcid.org/0000-0001-6833-7580
Gisela N. Ortiz-León https://orcid.org/0000-0002-2863-676X
Tomoaki Oyama https://orcid.org/0000-0003-4046-2923
Feryal Özel https://orcid.org/0000-0003-4413-1523
Daniel C. M. Palumbo https://orcid.org/0000-0002-7179-3816
Georgios Filippos Paraschos https://orcid.org/0000-0001-6757-3098
Jongho Park https://orcid.org/0000-0001-6558-9053
Harriet Parsons https://orcid.org/0000-0002-6327-3423
Nimesh Patel https://orcid.org/0000-0002-6021-9421
Ue-Li Pen https://orcid.org/0000-0003-2155-9578
Richard Plambeck https://orcid.org/0000-0001-6765-9609
Oliver Porth https://orcid.org/0000-0002-4584-2557
Ben Prather https://orcid.org/0000-0002-0393-7734
Jorge A. Preciado-López https://orcid.org/0000-0002-4146-0113
Dimitrios Psaltis https://orcid.org/0000-0003-1035-3240
Hung-Yi Pu https://orcid.org/0000-0001-9270-8812
Ramprasad Rao https://orcid.org/0000-0002-1407-7944
Mark G. Rawlings https://orcid.org/0000-0002-6529-202X
Alexander W. Raymond https://orcid.org/0000-0002-5779-4767
Luciano Rezzolla https://orcid.org/0000-0002-1330-7103
Angelo Ricarte https://orcid.org/0000-0001-5287-0452
Bart Ripperda https://orcid.org/0000-0002-7301-3908
Freek Roelofs https://orcid.org/0000-0001-5461-3687
Alan Rogers https://orcid.org/0000-0003-1941-7458
Eduardo Ros https://orcid.org/0000-0001-9503-4892
Cristina Romero-Cañizales https://orcid.org/0000-0001-6301-9073
Arash Roshanineshat https://orcid.org/0000-0002-8280-9238
Alan L. Roy https://orcid.org/0000-0002-1931-0135
Ignacio Ruiz https://orcid.org/0000-0002-0965-5463
Chet Ruszczyk https://orcid.org/0000-0001-7278-9707
Kazi L. J. Rygl https://orcid.org/0000-0003-4146-9043
Salvador Sánchez https://orcid.org/0000-0002-8042-5951
David Sánchez-Argüelles https://orcid.org/0000-0002-7344-9920
Miguel Sánchez-Portal https://orcid.org/0000-0003-0981-9664
Mahito Sasada https://orcid.org/0000-0001-5946-9960
Kaushik Satapathy https://orcid.org/0000-0003-0433-3585
Tuomas Savolainen https://orcid.org/0000-0001-6214-1085
Jonathan Schonfeld https://orcid.org/0000-0002-8909-2401
Karl-Friedrich Schuster https://orcid.org/0000-0003-2890-9454
Lijing Shao https://orcid.org/0000-0002-1334-8853

Zhiqiang Shen (沈志强) https://orcid.org/0000-0003-3540-8746
Des Small https://orcid.org/0000-0003-3723-5404
Bong Won Sohn https://orcid.org/0000-0002-4148-8378
Jason SooHoo https://orcid.org/0000-0003-1938-0720
Kamal Souccar https://orcid.org/0000-0001-7915-5272
He Sun (孙赫) https://orcid.org/0000-0003-1526-6787
Fumie Tazaki https://orcid.org/0000-0003-0236-0600
Alexandra J. Tetarenko https://orcid.org/0000-0003-3906-4354
Paul Tiede https://orcid.org/0000-0003-3826-5648
Remo P. J. Tilanus https://orcid.org/0000-0002-6514-553X
Michael Titus https://orcid.org/0000-0001-9001-3275
Pablo Torne https://orcid.org/0000-0001-8700-6058
Sascha Trippe https://orcid.org/0000-0003-0465-1559
Matthew Turk https://orcid.org/0000-0002-5294-0198
Huib Jan van Langevelde https://orcid.org/0000-0002-0230-5946
Daniel R. van Rossum https://orcid.org/0000-0001-7772-6131
Jesse Vos https://orcid.org/0000-0003-3349-7394
Jan Wagner https://orcid.org/0000-0003-1105-6109
Derek Ward-Thompson https://orcid.org/0000-0003-1140-2761
John Wardle https://orcid.org/0000-0002-8960-2942
Jonathan Weintroub https://orcid.org/0000-0002-4603-5204
Norbert Wex https://orcid.org/0000-0003-4058-2837
Robert Wharton https://orcid.org/0000-0002-7416-5209
Kaj Wiik https://orcid.org/0000-0002-0862-3398
Gunther Witzel https://orcid.org/0000-0003-2618-797X
Michael F. Wondrak https://orcid.org/0000-0002-6894-1072
George N. Wong https://orcid.org/0000-0001-6952-2147
Qingwen Wu (吴庆文) https://orcid.org/0000-0003-4773-4987
Paul Yamaguchi https://orcid.org/0000-0002-6017-8199
Doosoo Yoon https://orcid.org/0000-0001-8694-8166
André Young https://orcid.org/0000-0003-0000-2682
Ken Young https://orcid.org/0000-0002-3666-4920
Ziri Younsi https://orcid.org/0000-0001-9283-1191
Feng Yuan (袁峰) https://orcid.org/0000-0003-3564-6437
Ye-Fei Yuan (袁业飞) https://orcid.org/0000-0002-7330-4756
J. Anton Zensus https://orcid.org/0000-0001-7470-3321
Shuo Zhang https://orcid.org/0000-0002-2967-790X
Shan-Shan Zhao (赵杉杉) https://orcid.org/0000-0002-9774-3606

References

Abdollahi, S., Acero, F., Ackermann, M., et al. 2020, ApJS, 247, 33
Agudo, I., Thum, C., Gómez, J. L., & Wiesemeyer, H. 2014, A&A, 566, A59
Akiyama, K., Kuramochi, K., Ikeda, S., et al. 2017, ApJ, 838, 1
Aller, M. F., Aller, H. D., & Hughes, P. A. 2009, arXiv:0912.3176
Blackburn, L., Chan, C.-k., Crew, G. B., et al. 2019, ApJ, 882, 23
Blackburn, L., Pesce, D. W., Johnson, M. D., et al. 2020, ApJ, 894, 31
Bonning, E., Megan Urry, C., Bailyn, C., et al. 2012, ApJ, 756, 13
Broderick, A. E., Gold, R., Karami, M., et al. 2020a, ApJ, 897, 139
Broderick, A. E., Pesce, D. W., Tiede, P., Pu, H.-Y., & Gold, R. 2020b, ApJ, 898, 9
Chael, A. A., Johnson, M. D., Bouman, K. L., et al. 2018, ApJ, 857, 23
Chael, A. A., Johnson, M. D., Narayan, R., et al. 2016, ApJ, 829, 11
Deller, A. T., Brisken, W. F., Phillips, C. J., et al. 2011, PASP, 123, 275
Dong, L., Zhang, H., & Giannios, D. 2020, MNRAS, 494, 1817
EHTC, Akiyama, K., Alberdi, A., et al. 2019a, ApJL, 875, L1
EHTC, Akiyama, K., Alberdi, A., et al. 2019b, ApJL, 875, L2
EHTC, Akiyama, K., Alberdi, A., et al. 2019c, ApJL, 875, L3
EHTC, Akiyama, K., Alberdi, A., et al. 2019d, ApJL, 875, L4
EHTC, Akiyama, K., Alberdi, A., et al. 2022a, ApJL, 930, L12
EHTC, Akiyama, K., Alberdi, A., et al. 2022b, ApJL, 930, L13
EHTC, Akiyama, K., Alberdi, A., et al. 2022c, ApJL, 930, L14
EHTC, Akiyama, K., Alberdi, A., et al. 2022d, ApJL, 930, L15
EHTC, Akiyama, K., Algaba, J. C., et al. 2021, ApJL, 910, L12
Foschini, L., Pian, E., Maraschi, L., et al. 2006, A&A, 450, 77
Goddi, C., Martí-Vidal, I., Messias, H., et al. 2019, PASP, 131, 075003
Goddi, C., Martí-Vidal, I., Messias, H., et al. 2021, ApJL, 910, L14
Homan, D. C., Kovalev, Y. Y., Lister, M. L., et al. 2006, ApJL, 642, L115
Hunter, J. D. 2007, CSE, 9, 90
Issaoun, S., Johnson, M. D., Blackburn, L., et al. 2019, ApJ, 871, 30
Issaoun, S., Wielgus, M., Jorstad, S., et al. 2022, ApJ, 934, 145
Janssen, M., Goddi, C., van Bemmel, I. M., et al. 2019, A&A, 626, A75
Jorstad, S. G., Marscher, A. P., Larionov, V. M., et al. 2010, ApJ, 715, 362
Jorstad, S. G., Marscher, A. P., Lister, M. L., et al. 2005, AJ, 130, 1418
Jorstad, S. G., Marscher, A. P., Morozova, D. A., et al. 2017, ApJ, 846, 98
Jorstad, S. G., Marscher, A. P., Stevens, J. A., et al. 2007, AJ, 134, 799
Junkkarinen, V. 1984, PASP, 96, 539
Keck, M. 2019, PhD thesis, Boston University
Kharb, J.-Y., Krichbaum, T. P., Broderick, A. E., et al. 2020, A&A, 640, A69
Kharb, P., Lister, M. L., & Cooper, N. J. 2010, ApJ, 710, 764
Lee, S.-S. 2013, JKAS, 46, 243
Liang, E. W., & Liu, H. T. 2003, MNRAS, 340, 632
Liodakis, I., Hovatta, T., Huppenkothen, D., et al. 2018, ApJ, 866, 137
Lister, M. L., Aller, D. C., Hovatta, T., et al. 2019, ApJ, 874, 43
Lister, M. L., Aller, M. F., Aller, H. D., et al. 2016, AJ, 152, 12
Lu, R.-S., Krichbaum, T. P., & Zensus, J. A. 2011, MNRAS, 418, 2260
Martí-Vidal, I., Mus, A., Janssen, M., de Vicente, P., & González, J. 2021, A&A, 646, A52
Martí-Vidal, I., Vlemmings, W. H. T., & Muller, S. 2016, A&A, 593, A61
Pacholczyk, A. G. 1970, Series of Books in Astronomy and Astrophysics (San Francisco: Freeman)
Pesce, D. W. 2021, AJ, 161, 178
Planck Collaboration, Ade, P. A. R., Aghanim, N., et al. 2016, A&A, 594, A13
Pushkarev, A. B., Aller, M. F., Aller, H. D., et al. 2022, arXiv:2209.04842
Ramakrishnan, V., Hovatta, T., Nieppola, E., et al. 2015, MNRAS, 452, 1280
Readhead, A. C. S. 1994, ApJ, 426, 51
Salvatier, J., Wiecki, T. V., & Fonnesbeck, C. 2016, PeerJ Comp. Sci., 2, e55
Shepherd, M. C. 1997, in ASP Conf. Ser. 125, Astronomical Data Analysis Software and Systems VI, ed. G. Hunt & H. E. Payne (San Francisco, CA: ASP), 77
van der Walt, S., Colbert, S. C., & Varoquaux, G. 2011, CSE, 13, 22
Wardle, J. F. C., Homan, D. C., Ojha, R., & Roberts, D. H. 1998, Natur, 395, 457
Weaver, Z. R., Jorstad, S. G., Marscher, A. P., et al. 2022, ApJS, 260, 12
Wielgus, M., Marchili, N., Martí-Vidal, I., et al. 2022, ApJL, 930, L19
Williamson, K. E., Jorstad, S. G., Marscher, A. P., et al. 2014, ApJ, 789, 135